The Astrophysical Journal, 863:44 (23pp), 2018 August 10 https://doi.org/10.3847/1538-4357/aab846

Disks around T Tauri Stars with SPHERE (DARTTS-S). I. SPHERE/IRDIS Polarimetric Imaging of Eight Prominent T Tauri Disks*

Henning Avenhaus[1,2,3], Sascha P. Quanz[2,13], Antonio Garufi[4], Sebastian Perez[3,5], Simon Casassus[3,5], Christophe Pinte[6,7], Gesa H.-M. Bertrang[3], Claudio Caceres[8,9], Myriam Benisty[10,11], and Carsten Dominik[12]

[1] Max Planck Institute for Astronomy, Königstuhl 17, D-69117 Heidelberg, Germany; havenhaus@gmail.com
[2] ETH Zurich, Institute for Particle Physics and Astrophysics, Wolfgang-Pauli-Strasse 27, CH-8093 Zurich, Switzerland
[3] Departamento de Astronomía, Universidad de Chile, Casilla 36-D, Santiago, Chile
[4] Universidad Autonónoma de Madrid, Dpto. Física Teórica, Módulo 15, Facultad de Ciencias, E-28049 Madrid, Spain
[5] Millennium Nucleus Protoplanetary Disks Santiago, Chile
[6] Monash Centre for Astrophysics (MoCA) and School of Physics and Astronomy, Monash University, Clayton VIC 3800, Australia
[7] Univ. Grenoble Alpes, CNRS, IPAG, F-38000 Grenoble, France
[8] Departamento de Ciencias Fisicas, Facultad de Ciencias exactas, Universidad Andres Bello, Av. Fernandez Concha 700, Santiago, Chile
[9] Núcleo Milenio Formación Planetaria—NPF, Universidad de Valparaíso, Av. Gran Bretaña 1111, Valparaíso, Chile
[10] Unidad Mixta Internacional Franco-Chilena de Astronomía, CNRS/INSU UMI 3386 and Departamento de Astronomía, Universidad de Chile, Casilla 36-D, Santiago, Chile
[11] Univ. Grenoble Alpes, CNRS, IPAG, F-38000 Grenoble, France
[12] Astronomical Institute Anton Pannekoek, University of Amsterdam, The Netherlands
Received 2018 January 26; revised 2018 March 9; accepted 2018 March 18; published 2018 August 8

Abstract

We present the first part of our Disks ARound T Tauri Stars with SPHERE (DARTTS-S) survey: observations of eight T Tauri stars that were selected based on their strong (sub)millimeter excesses using SPHERE/IRDIS polarimetric differential imaging in the *J* and *H* bands. All observations successfully detect the disks, which appear vastly different in size, from ≈80 au in scattered light to >400 au, and display total polarized disk fluxes between 0.06% and 0.89% of the stellar flux. For five of these disks, we are able to determine the three-dimensional structure and the flaring of the disk surface, which appears to be relatively consistent across the different disks, with flaring exponents α between ≈1.1 and ≈1.6. We also confirm literature results with regard to the inclination and position angle of several of our disks and are able to determine which side is the near side of the disk in most cases. While there is a clear trend of disk mass with stellar ages (≈1 to >10 Myr), no correlations of disk structures with age were found. There are also no correlations with either stellar mass or submillimeter flux. We do not detect significant differences between the *J* and *H* bands. However, we note that while a high fraction (7/8) of the disks in our sample show ring-shaped substructures, none of them display spirals, in contrast to the disks around more massive Herbig Ae/Be stars, where spiral features are common.

Key words: planet–disk interactions – protoplanetary disks – stars: formation – stars: pre-main sequence

1. Introduction

Significant progress has been made in recent years in providing empirical constraints on the physical and chemical properties of circumstellar disks, the cradles of future planetary systems, thanks to high spatial resolution observations. At (sub) millimeter wavelengths, ALMA has been revolutionizing our understanding of the spatial distribution and properties of larger (millimeter-sized) dust grains, primarily found in the midplane of circumstellar disks, and the molecular gas components (e.g., ALMA Partnership et al. 2015; Andrews et al. 2016; Huang et al. 2017; Pinte et al. 2017; van der Plas et al. 2017). At optical/near-infrared wavelengths, polarimetric differential imaging (PDI) observations with adaptive optics (AO)-assisted, high-resolution, and high-contrast cameras on 8 m class telescopes have been yielding unprecedented images of the disks' surface layer by tracing scattering off the smaller (micron-sized) dust grains (e.g., Hashimoto et al. 2011; Mayama et al. 2012; Avenhaus et al. 2014a, 2014b; Garufi et al. 2014; Thalmann et al. 2015; Akiyama et al. 2016; Monnier et al. 2017; Bertrang et al. 2018), with the new SPHERE/IRDIS instrument being particularly successful at imaging disks at high signal-to-noise ratio (S/N; e.g., Pohl et al. 2017; Stolker et al. 2017). An overview of recent SPHERE results can be found in Garufi et al. (2017a). Both techniques revealed a previously unknown richness and diversity in disk morphology and substructure. One of the key questions is to what extent these structures are leading to or are the result of planet formation processes. While the ALMA community has been publishing papers investigating single sources in greater detail, as well as surveys with dozens of sources (albeit with lower spatial resolution and sensitivity; e.g., Carpenter et al. 2014), the high-contrast-imaging community was largely focusing on individual targets and, in addition, primarily on Herbig Ae/Be stars (e.g., Garufi et al. 2016; Ginski et al. 2016; Ohta et al. 2016; Avenhaus et al. 2017). There are ongoing activities starting to investigate larger samples of (Herbig Ae/Be) objects in order to understand evolutionary pathways (e.g., Ababakr et al. 2017; Garufi et al. 2017b), but these studies are still rare. In addition, while some PDI studies also investigated the properties of T Tauri disks (e.g., Oh et al. 2016a, 2016b; van Boekel et al. 2017), disks around Herbig stars were easier targets, as they are generally larger in extent and brighter in scattered light. Furthermore, the

* Based on observations collected at the European Organisation for Astronomical Research in the Southern Hemisphere, Chile, under program 096.C-0523(A).
[13] National Center of Competence in Research "PlanetS" (http://nccr-planets.ch).

Table 1
Target Overview

Target	Alt. Name	Sp. Type	R (mag)	J (mag)	H (mag)	Distance (pc)	$f_{1.3\,\mathrm{mm}}$ (mJy)	$\dot{M}$ ($M_\odot$ yr^{-1})
IM Lup	Sz 82	M0	≈10.8	8.783(21)	8.089(40)	158.45 ± 1.34	200 (1)	$1{\cdot}10^{-11}$ (I)
RXJ 1615	RX J1615.3–3255	K5	11.21	9.435(24)	8.777(23)	157.69 ± 0.89	132 (2)	$3{\cdot}10^{-9}$ (II)
RU Lup	Sz 83	K7/M0	≈10.2	8.732(26)	7.824(42)	159.57 ± 1.71	197 (3)	$6{\cdot}10^{-8}$ (III)
MY Lup	PDS 77	K0	11.06(5)	9.457(26)	8.690(30)	156.58 ± 1.17	56 (4)	$<2{\cdot}10^{-10}$ (III)
PDS 66	MP Mus	K1	≈10.0	8.277(32)	7.641(23)	98.86 ± 0.30	224 (5)	$1.3{\cdot}10^{-10}$ (IV)
V4046 Sgr	Hen 3-1636	K5+K7	≈10.3	8.071(23)	7.435(51)	72.41 ± 0.34	283 (6)	$2{\cdot}5{\cdot}10^{-10}$ (V)
DoAr 44	V2062 Oph	K3	11.70	9.233(23)	8.246(57)	145.91 ± 0.99	105 (7)	$6{\cdot}10^{-9}$ (II)
AS 209	V1121 Oph	K4	≈11.1	8.302(39)	7.454(24)	120.98 ± 0.91	300 (8)	$1.3{\cdot}10^{-7}$ (VI)

Note. Overview of our targets along with literature values. Spectral types and magnitudes are from SIMBAD. The R magnitudes are given for reference, as the SPHERE AO is driven in the R band. Where no R magnitude is available, we roughly estimated it from the available magnitudes (indicated by "≈"); however, all of our targets are variable to some degree. Note that V4046 Sgr is a spectroscopic binary and, furthermore, has a wide-separation binary companion (Kastner et al. 2011).
References. Distances and 1σ errors are from Gaia Collaboration et al. (2018). Additional distance references used in the writing of this paper: Krautter et al. (1997), Comerón (2008), Torres et al. (2008), Andrews et al. (2011). 1.3 mm flux references: (1) Cleeves et al. (2016), (2) van der Marel et al. (2015), (3) van Kempen et al. (2007), (4) Lommen et al. (2010), (5) Schütz et al. (2005), (6) Rosenfeld et al. (2013), (7) Nuernberger et al. (1998), (8) Andre & Montmerle (1994). Accretion rate references: (I) Günther et al. (2010), (II) Manara et al. (2014), (III) Alcalá et al. (2017), (IV) Ingleby et al. (2013), (V) Donati et al. (2011), (VI) Johns-Krull et al. (2000).

generally brighter host star makes driving an AO easier. However, while Herbig Ae/Be stars are more massive and hence more rare, T Tauri stars (the progenitors of solar-like and lower-mass stars) are significantly more common. In order to derive a comprehensive picture of circumstellar disk properties and identify correlations possibly related to disk evolution scenarios, larger samples across a wide range of stellar masses need to be studied in both scattered light and (sub)millimeter emission.

Disks ARound T Tauri Stars (DARTTS) is an effort at understanding T Tauri disks in both scattered light and submillimeter, combining the power of SPHERE/IRDIS and ALMA to investigate disk structures at different wavelengths and similar high resolution. This paper presents the results for the first eight sources of our DARTTS-S[14] project, which is aimed presenting and analyzing a comprehensive NIR data set of PDI observations of T Tauri stars. It gives an overview of our results. Part of the DARTTS-S data for DoAr 44 is presented and analyzed in detail in Casassus et al. (2018), while further papers analyzing data for specific sources are in preparation.

Thanks to its AO performance and sensitivity, VLT SPHERE/IRDIS is able to detect and reveal circumstellar disks even around low-mass stars with apparent magnitudes of $R \approx 10$–13 mag. Here we focus on the first eight targets (see Table 1) and give a general overview of the observations, data reduction (including a detailed description of the updated data reduction pipeline), and first quantitative results. Because the amount of data obtained is large, in-depth analysis and modeling of individual targets will be done in dedicated follow-up papers. However, the coherent observation technique and similar S/N allow us to discuss first general trends and make comparisons across our target sample.

2. Our Targets

The first eight targets of our sample were selected based on (sub)millimeter brightness. We chose to select those stars that have an extraordinarily high (sub)millimeter flux, making sure to at the same time select stars covering a wide range of ages. The target list is thus not an unbiased selection of T Tauri stars but rather a selection aimed at maximizing chances for detection. Some of the objects have previously been detected in scattered light. Literature values for the spectral types, distances, and *R/J/H* band magnitudes, as well as 1.3 mm photometry, can be found in Table 1. We derive age and stellar/disk mass estimates in Section 5.1 using pre-main-sequence tracks and submillimeter luminosities. Our targets in detail are as follows.

2.1. IM Lup

IM Lup is a well-studied M0 star located in the Lupus 2 cloud classified as a weak-line T Tauri star (WTTS) with weak accretion (Padgett et al. 2006; Günther et al. 2010). It is a bright millimeter source as detected by SMA (Pinte et al. 2008) and ATCA (Lommen et al. 2007), which indicates the presence of dust grains of several millimeters in size, with a dust mass of $\approx 10^{-3}\,M_\odot$. The disk is inclined by 54° ± 3° and can be traced in molecular gas emission to ≈750 au, with a break in the gas and dust density profile at ≈330 au (Panić et al. 2009). Two rings are seen in the DCO^+ (3–2) line at radii of ≈320 and ≈95 au, the inner of which can be connected to the CO snow line, while the outer can be explained by nonthermal CO desorption at the position where the optical thickness of the disk decreases. Strong silicate features in the spectrum suggest the presence of micron-sized dust grains at the disk surface, which, together with the millimeter data, suggests spatial segregation of the dust grains as a function of size, for example from dust settling (Panić et al. 2009; Öberg et al. 2011, 2015).

The disk is revealed with *Hubble Space Telescope* (*HST*) scattered-light imaging, where the outer radius of the scattered-light disk can be shown to be ≈335 au, with a faint halo extending out to ≈700 au. Modeling of the system requires a flared disk (flaring exponent 1.13–1.17) with a scale height of 10 au at a distance of 100 au, and color measurements show a chromaticity of the disk between 0.6 and 1.6 μm that cannot be reproduced by simple scattering on spheres, suggesting the presence of aggregates on the disk surface (Pinte et al. 2008). The latest available ALMA measurements show that the CO disk possibly extends even further, to ≈950 au in radius, making this one of the largest known protoplanetary disks with a disk mass of $M_{\mathrm{gas}} \approx 0.17\,M_\odot$ (Pinte et al. 2017). These authors also confirmed the sharp truncation of millimeter disk

[14] Disks ARound T Tauri Stars with SPHERE; PI: H. Avenhaus. The accompanying ALMA investigation of these disks under the DARTTS-A program is led by S. Perez.

emission at smaller radii (≈295 au) and showed that it is also possible to directly measure radial and vertical temperature gradients in the disk. All distances mentioned here have been scaled to the new *Gaia* distance estimate of 158.45 pc (see Table 1). Several models for the available data exist in the literature (Pinte et al. 2008; Panić et al. 2009; Cleeves et al. 2016).

2.2. RXJ 1615

RX J1615.3–3255, which we abbreviate in this paper as RXJ 1615, is a WTTS located in an ≈1 Myr old part of the Lupus cloud (Krautter et al. 1997; Makarov 2007). It is identified as a transition disk, with modeling of high-resolution submillimeter data and *Spitzer* IR spectroscopy pointing toward an inner hole extending clearly beyond the sublimation radius (based on the lack of near-IR excess) and a not fully cleared but low-density cavity out to ≈25 au (Merín et al. 2010; Andrews et al. 2011). The latter authors also determined the total mass of the disk, assuming a gas-to-dust ratio of 100, to be as high as 0.128 $M_\odot$, but the accretion rate ($4 \cdot 10^{-10} M_\odot\,\mathrm{yr}^{-1}$) is the lowest of all measured targets in their sample. Newer work gives a significantly higher accretion rate, though ($3 \cdot 10^{-9} M_\odot\,\mathrm{yr}^{-1}$; Manara et al. 2014). The characteristic radius of the disk (as seen in the submillimeter continuum) is 98 au, with an inclination estimate of ≈41°.

More recently, the disk was resolved through high-contrast imaging with VLT/SPHERE, both in polarization (with IRDIS and ZIMPOL PDI) and total intensity (using IRDIS and IFS ADI) by de Boer et al. (2016), who determined a disk inclination of $i = 47° \pm 2°$ and were able to resolve multiple rings at 1.″50, 1.″06, and 0.″30 (237/167/47 au), as well as another arc further out that they could not clearly determine to be either the rear surface of the disk or another ring. Earlier, Kooistra et al. (2017) were able to image the disk using Subaru/HiCIAO PDI, albeit at significantly lower S/N, not being able to detect any of the disk rings and tracing the disk out to only ≈58 au. However, they were able to show that small dust grains must extend into the cavity seen in the submillimeter in order to be able to produce the scattered-light signature seen in their observations and suggested that the small dust grain population must be radially decoupled from the larger grains. Neither of the observations was able to detect the inner gap in scattered light, despite the fact that the inner working angle in both cases was smaller than the ≈25 au of the submillimeter cavity size. All distances mentioned here have been scaled to the new Gaia distance estimate of 157.69 pc (see Table 1) .

2.3. RU Lup

RU Lup is one of the most active and well-studied T Tauri stars (Lamzin et al. 1996; Stempels & Piskunov 2002; Herczeg et al. 2005). This young object (≈1 Myr; Siwak et al. 2016) is located inside the Lupus 2 cloud (de Zeeuw et al. 1999; Comerón 2008). Its stellar mass is estimated to be slightly subsolar (0.6–0.7 $M_\odot$; Stempels & Piskunov 2002) with a high accretion rate of $6 \cdot 10^{-8} M_\odot\,\mathrm{yr}^{-1}$ (Alcalá et al. 2017). Spectral line broadening, as well as blueshifted emission-line signatures, indicate that RU Lup is observed at a low inclination angle (Siwak et al. 2016). The star exhibits variations in radial velocity with a periodicity of 3.7 days, which was first interpreted as an indication for an ≈0.05 $M_\odot$ brown dwarf companion on a tight orbit by Gahm et al. (2005). However, the variations were later found to be more likely explained by the presence of large spots or groups of spots on the surface of RU Lup itself, while a low-mass companion or stellar pulsations as a source for these variations were discussed as unlikely (Stempels et al. 2007). Nevertheless, RU Lup shows signs of an inner gap on au scales that could be opened by a Jupiter-like companion (Takami et al. 2003). Its disk has not been imaged in scattered light before.

2.4. MY Lup

MY Lup is a K0 T Tauri star located in the Lupus IV star-forming region (Hughes et al. 1993; Comerón 2008; Alcalá et al. 2017). It has been identified as a transition disk and a potential candidate for ongoing planet formation (Romero et al. 2012).

The disk has been observed previously by ALMA, where the inclination was determined to be ∼73° (Ansdell et al. 2016), suggesting that it may be partially obscured by its circumstellar disk. Spectroscopic measurements have determined a remarkably low accretion rate as compared with similar disks in Lupus (Alcalá et al. 2017; Frasca et al. 2017). This is consistent with the finding of a rather low gas-to-dust mass ratio from faint CO isotopologue ALMA observations (Miotello et al. 2017). So far, there are no studies of the disk in scattered light.

2.5. PDS 66

PDS 66 (also referred to as MP Mus) is a K1 classical T Tauri star and one of the most nearby pre-main-sequence stars. The recent *Gaia* measurement of $d = 98.86 \pm 0.30$ pc (*Gaia* Collaboration et al. 2018) supports its membership in the ϵ Cha association proposed by Murphy et al. (2013). The disk of PDS 66 was first imaged in scattered light with *HST*/NICMOS by Cortes et al. (2009), who estimated an outer radius of 170 au (with a distance estimate of 86 pc, translating to 195 au at the updated *Gaia* distance) and an inclination of $32° \pm 5°$. Their spectral energy distribution (SED) fitting suggested a disk inner edge at the dust sublimation temperature, though partial clearing may have happened already. More recent Gemini Planet Imager (GPI) images in PDI (Wolff et al. 2016) revealed a ringlike structure at 78 au separated from a bright inner disk by a 29 au wide region with diminished flux (radii have been updated with the new *Gaia* distance).

The total dust mass of the disk is around $5 \cdot 10^{-5} M_\odot$ (Carpenter et al. 2005). A lower limit for the gas mass from CO measurements was given by Kastner et al. (2010) at $9 \cdot 10^{-6} M_\odot$, with the molecular gas disk extending out to ≈119 au (again converted using the new *Gaia* distance estimate).

2.6. V4046 Sgr

V4046 Sgr is a close binary system with two K dwarfs of almost equal mass on a 2.4 day orbit (Quast et al. 2000; Stempels & Gahm 2004). There is also a wide-separation (2.″82) binary that is likely loosely bound to the system (Kastner et al. 2011). The SED in the IR shows a strong minimum between 5 and 8 μm, typical for transition disks, and a silicate dust emission feature from large amorphous grains is present (e.g., Rapson et al. 2015b). Studies of the disk at 1.3 mm using ALMA reveal dust emission confined to a narrow ring centered at a radius of 37 au with a central hole of a radius

of $r = 29$ au. This dust ring is embedded in a larger CO gas disk with an inclination of $\approx 33.^{\circ}5$ at a position angle of $\approx 76^{\circ}$ and extending out to 300 au (Rosenfeld et al. 2012, 2013). V4046 Sgr is a quite isolated young system at a distance of ≈ 73 pc. It is most likely a member of the β Pic moving group (Torres et al. 2008) and therefore about 23 Myr old (Mamajek & Bell 2014), making it the oldest system in our sample. V4046 Sgr is a special object: not only is it the only gas-rich disk in the β Pic moving group, but it also resembles a Herbig Ae system in terms of the total mass of the two central objects, while in terms of luminosity, it behaves like a T Tauri system.

Disk images taken in polarized light by GPI were presented by Rapson et al. (2015a). These authors reported a central cavity inside ≈ 10 au, a ring with maximum flux around ≈ 14 au, and a gap at ≈ 20 au, as well as an outer halo extending to ≈ 45 au. The distances have not been re-calculated given the very small difference between the old distance estimate (73 pc, Torres et al. 2008) and the new one (72.41 ± 0.34 pc, Gaia collaboration et al. 2018).

2.7. DoAr 44

DoAr 44 is a transition disk associated with ρ Ophiuchus (Andrews et al. 2011). Like most T Tauri stars, it is actively accreting, and Manara et al. (2014) derived the accretion rate to be $\approx 6 \cdot 10^{-9}\, M_{\odot}\, \mathrm{yr}^{-1}$, one of the higher accretion rates among the 22 transition disks in their sample.

The ALMA Band 7 continuum (275–370 GHz/0.8–1.1 mm; van der Marel et al. 2016) reveals a fairly axially symmetric ring at a radius of $0.''3$, which is inclined by $\approx 20^{\circ}$ along a P.A. of $\approx 60^{\circ}$. The total dust mass inferred from the continuum is $5 \cdot 10^{-5}\, M_{\odot}$, while the gas mass inferred from the rare CO isotopologues is $2.5 \cdot 10^{-3}\, M_{\odot}$.

A subset of the DoAr 44 scattered-light observations is presented in Casassus et al. (2018), who proposed a warped geometry to explain the polarized intensity. Here we place this object in context with the other sources.

2.8. AS 209

AS 209 is a classical T Tauri star (spectral type K5; Pérez et al. 2012) with a high accretion rate of $1.3 \cdot 10^{-7}\, M_{\odot}\, \mathrm{yr}^{-1}$ (Johns-Krull et al. 2000). The star is associated with the ρ Ophiuchus cloud but dwells in isolation from the main cloud members. AS 209 has a circumstellar disk that appears optically thin in continuum emission between 0.8 and 9.0 mm. The disk has a radius of $\approx 1''$ at 0.88 mm and becomes more compact at longer wavelengths. Pérez et al. (2012) modeled these millimeter data, finding evidence for radial variations of dust opacity at $0.''2$–$0.''5$ resolution. It is inclined by $\approx 38^{\circ}$ along a P.A. of $\approx 86^{\circ}$ (Andrews et al. 2009).

ALMA observations of CO isotopologues report a ringlike CO enhancement at $\approx 1''$, possibly linked to CO desorption near the edge of AS 209's disk (Huang et al. 2016). More recent data, also from ALMA (Fedele et al. 2017), are able to identify two rings at ≈ 72 and ≈ 124 au around a central core of emission, with gaps between them at ≈ 59 and ≈ 98 au at 2:1 resonance radii (distances have been recalculated using the new Gaia distance estimate of 120.98 pc; see Table 1). The outer of these gaps is consistent with an approximately Saturn-mass planet opening it, while any planet in the inner gap would have to be less massive ($<0.1\, M_{\mathrm{Jup}}$). These ALMA data are also able to constrain the inclination and position angle more strictly, at $35.^{\circ}3 \pm 0.^{\circ}8$ and $86.^{\circ}0 \pm 0.^{\circ}7$, respectively.

There is no scattered-light image of the disk available in the literature.

3. Observations and Data Reduction

All data presented in this paper were obtained during the six nights of 2016 March 10–15 using SPHERE/IRDIS (Beuzit et al. 2008; Dohlen et al. 2008) on the ESO Very Large Telescope (VLT). IRDIS was used in DPI mode (Langlois et al. 2014) in both the J and H bands, together with the N_ALC_YJH_S coronagraph. Depending on the brightness of the source, either 32 or 64 s integration times were used for the individual frames in order not to saturate the detector outside the coronagraph edge. Each observation followed the same pattern: flux frame (to measure the stellar flux and the point-spread function (PSF))—centering frame (to determine the exact position of the star behind the coronagraph)—science observations—second centering frame. No sky frames were taken. The total exposure times for the total of 16 observations (eight sources in two bands each) varied depending on the sky conditions and scheduling. The exact on-source times for each source/filter combination can be found in Table 2.

The data reduction (see the Appendix) follows the general ideas presented in Avenhaus et al. (2014b), adapted for the IRDIS instrument and updated and improved where necessary. Specifically worth mentioning is the new way of correcting for instrumental polarization, which combines the equalizing of the ordinary and extraordinary beam with the technique of adding/subtracting scaled versions of the intensity frame to the Stokes Q and U parameters, pioneered by the SEEDS team (e.g., Follette et al. 2015). Together with allowing for a polarized sky background component, this results in an overall better correction for instrumental effects.

There is self-cancellation flux loss close to the star due to the finite spatial resolution (i.e., the finite size of the PSF) combined with the fact that the local Stokes parameter Q_{ϕ} (or P) cannot be measured directly; only the Stokes parameters Q and U can. This was first described in Avenhaus et al. (2014a) and is independent of the decomposition into the local Stokes vectors Q_{ϕ} and U_{ϕ}; i.e., it already occurs in the Q and U frames. However, there are other side effects to this decomposition that have not yet been described in the literature. The patterns produced specifically in the U_{ϕ} image by these effects can closely resemble signals that one would expect from multiple scattering events (e.g., Canovas et al. 2015), which means that it is easy to misinterpret them.

We describe both the origin of this effect, which we call Q_{ϕ}/U_{ϕ} cross-talk, and the way we correct for it (at the same time correcting for self-cancellation close to the star) in the Appendix, where we also describe the entire data reduction pipeline in detail again.

4. Results and Analysis

We successfully detect all eight T Tauri disks in both the J and H bands, though the detection in the J band for some sources was only possible at low S/N. We present an overview of the higher-S/N H-band data for all eight disks using logarithmic color maps in Figure 1. The disks have been scaled in such a way that they represent the same physical scale. It is clear that the disks are of vastly different physical sizes, with

Table 2
Observation Overview

Target	Filter	DIT (s)	NDIT	NCYCLE	Total Frames	Total Time (s)	Airmass	Seeing (arcsec)	τ_0 (ms)	Observation Date
	BB_J	64	2	7	56 (56)	3584 (3584)	1.04–1.14	0.73–0.98	1.0–2.0	2016 Mar 11
IM Lup										
	BB_H	64	2	6	48 (48)	3072 (3072)	1.07–1.16	1.07–1.52	2.7–4.1	2016 Mar 13
	BB_J	64	2	6	48 (48)	3072 (3072)	1.16–1.34	0.88–1.26	1.3–3.0	2016 Mar 14
RXJ 1615										
	BB_H	64	2	10.5	82 (80)	5376 (5120)	1.01–1.14	0.86–1.29	1.5–3.6	2016 Mar 14
	BB_J	64	2	9	72 (40)	4608 (2560)	1.02–1.05	1.31–2.20	0.7–1.3	2016 Mar 11
RU Lup										
	BB_H	64	2	8	64 (64)	4096 (4096)	1.04–1.13	1.08–1.47	1.6–2.7	2016 Mar 12
	BB_J	64	2	5	40 (40)	2560 (2560)	1.05–1.08	0.79–1.07	1.9–2.9	2016 Mar 15
MY Lup										
	BB_H	64	2	5	40 (35)	2560 (2240)	1.07–1.15	0.65–0.77	3.0–4.3	2016 Mar 15
	BB_J	64	2	6	48 (48)	3072 (3072)	1.42–1.46	1.01–1.27	1.9–3.0	2016 Mar 14
PDS 66										
	BB_H	64	2	7	56 (56)	3584 (3584)	1.41–1.44	0.84–1.04	2.2–3.3	2016 Mar 15
	BB_J	64	2	6	48 (48)	3072 (3072)	1.10–1.24	1.27–1.70	1.4–2.0	2016 Mar 12
V4046 Sgr										
	BB_H	64	2	6	48 (48)	3072 (3072)	1.05–1.15	0.89–1.19	1.8–2.7	2016 Mar 13
	BB_J	64	2	6	48 (48)	3072 (3072)	1.01–1.08	0.72–0.86	2.8–4.5	2016 Mar 13
DoAr 44										
	BB_H	64	2	5	40 (40)	2560 (2560)	1.01–1.05	0.84–1.07	2.4–3.8	2016 Mar 15
	BB_J	64	2	8	64 (64)	4096 (4096)	1.08–1.25	1.04–1.37	1.5–1.9	2016 Mar 10
AS 209										
	BB_H	32	4	4	64 (64)	2048 (2048)	1.01–1.02	0.73–0.91	2.7–3.6	2016 Mar 14

Note. Overview of our observations. The data were taken in PDI cycles, rotating through the four relevant half-wave-plate (HWP) positions. In each cycle, *NDIT* integrations with an integration time of *DIT* were taken before moving on to the next HWP position, for a total integration time of $NDIT^*DIT^*4$ per cycle. A total of *NCYCLE* of such cycles were taken, resulting in the total on-source integration time reported in the table. Since some frames were corrupted (for example, because the AO could not stabilize the PSF), not all data were usable for all observations. The numbers in parentheses represent the actual number of frames/integration time used in our data reduction. In the case of the *H*-band observations of RXJ 1615, one cycle aborted after being half-finished, resulting in a noninteger cycle number. Airmass, seeing, and coherence time are as reported by the instrument. For the seeing, the IA detector linear fit estimate is reported.

IM Lup being the largest and RU Lup, almost identical in mass and of the same age, being one of the smallest.

We also show our results in the more established way, where the data is multiplied by r2 (Figure 2). There, we also present the *J*-band and U_ϕ data. All disks except RU Lup show easily visible substructure (see also Figures 1 and 2). However, it is unlikely that the tightly spaced rings in AS 209 are real, because they only appear in the *H* band and the depressions in the Q_ϕ image coincide with the diffraction rings in the intensity image. We discuss this in Section 5.2.8. There are, however, fainter structures in this disk that are hard to identify by eye, which we discuss in more detail in the same section.

4.1. Surface Brightnesses

To get a first quantitative handle on the scattered light of the disks, we compare the brightness of their reflected, polarized light. Despite their different structures, inclinations, host star magnitudes, and distances, we calibrate all of our data with respect to the host star brightness. This way, we can compare how much of the incident starlight the disks reflect in total, keeping in mind that this figure is affected by the inclination of the disk. By comparing the *J* and *H* bands, we can get a rough estimate of the scattering color of the dust grains. Given the fact that we correct for the self-cancellation effect (as described above), we expect this figure not to be systematically affected by the difference in quality of the PSF between the *J* and *H* bands. This figure also does not need to be corrected for distance, as both the stellar and the disk flux, as observed from Earth, scale the same with distance. We do have to keep in mind, though, that any parts of the disk and their flux that are behind the coronagraph cannot be accounted for.

In Table 3, we show the ratio between the reflected light of our disks and the total intensity flux of the star–disk system. We measure the polarized flux in an annulus between the edge of the coronagraph and a radius of $3\farcs5$. Despite the fact that IM Lup, RXJ 1615, and, to a lesser extent, PDS 66 appear significantly larger than the other disks, this does not mean that they reflect more light than, e.g., DoAr 44, one of the smallest disks in our sample. RU Lup, also very small, is in fact also very faint, but the disk goes down to the coronagraph edge, and more flux could be hidden from view under the coronagraph (the majority of the polarized flux usually comes from the innermost regions of the disk). The same is true for AS 209, which is also faint but can actually be traced to about 200 au (see Figure 3). The third-faintest disk, PDS 66, is also the third disk in our sample where it is known that the disk extends very close to the star.

The brightest disk in our sample, by this measure, is MY Lup. However, this could be misleading, as MY Lup is highly inclined and the star likely shines partially through the disk, dimming the star (and thus decreasing the contrast between the star and the disk, making the disk relatively brighter). This interpretation goes well with the fact that the disk is apparently brighter in the *J* band than in the *H* band—a reddening of the star due to dust extinction would have exactly this effect. It is also in line with the relatively high extinction of

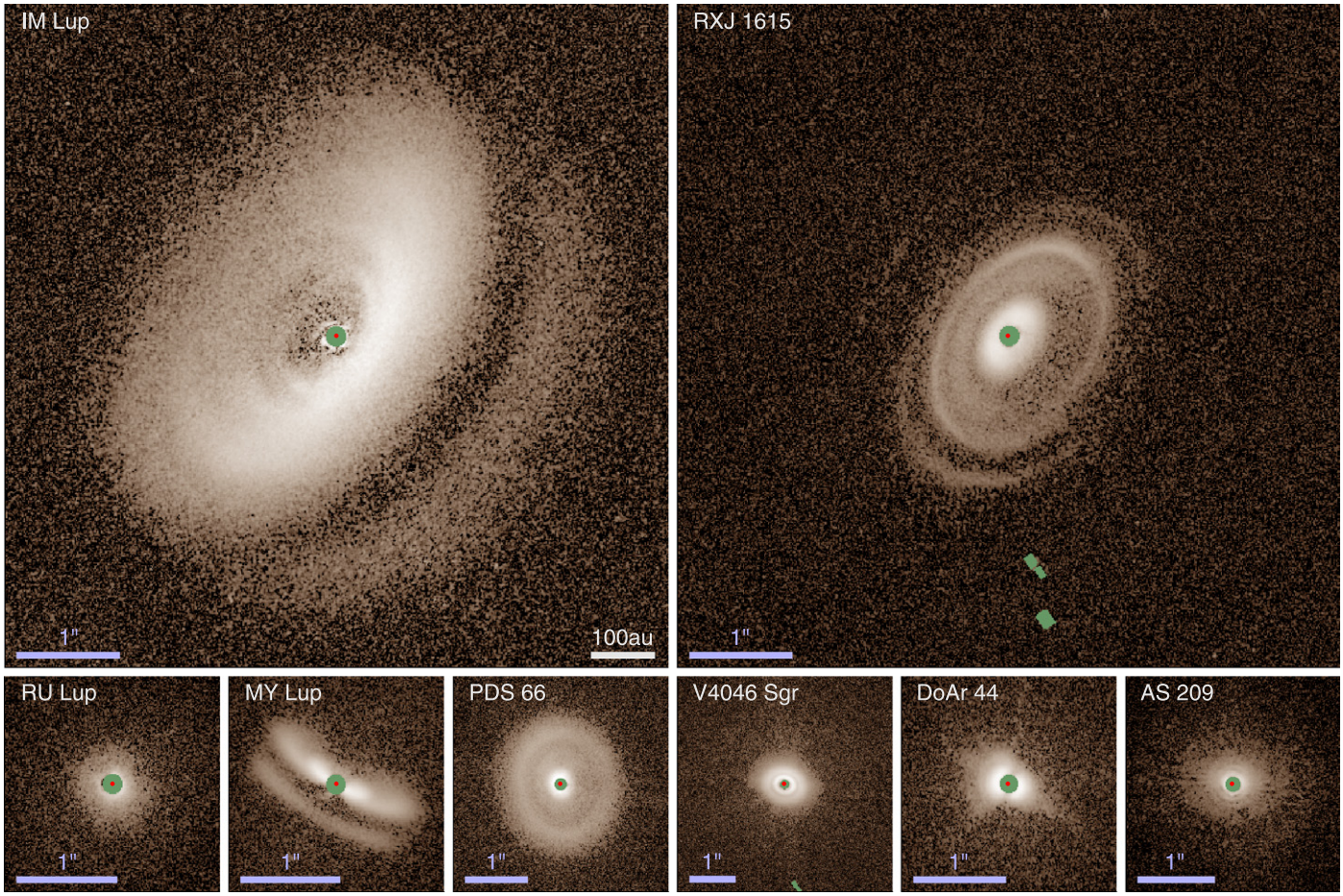

Figure 1. The *H*-band images displayed in logarithmic stretch (the exact stretch is adjusted for each disk individually to improve the visibility of substructures). The data were rescaled to represent the same physical size; thus, the 100 au scale bar in the first panel applies for all panels. Because the angular scales are different, a 1″ bar is shown in each panel. Immediately obvious is the extraordinary size of the IM Lup disk compared to the others, with RXJ 1615 coming in second. Areas in green represent places where no information is available (due to either being obscured by the coronagraph or bad detector pixels). The red dot in the center marks the position of the star. North is up and east is to the left in all frames.

Table 3
Ratio of Polarized Disk Flux vs. Stellar Flux

Target	*J* Band	*H* Band	*J/H* Ratio
IM Lup	0.53% ± 0.06%	0.66% ± 0.05%	0.81 ± 0.12
RXJ 1615	0.52% ± 0.13%	0.67% ± 0.32%	0.78 ± 0.42
RU Lup	0.06% ± 0.03%	0.12% ± 0.06%	0.51 ± 0.37
MY Lup	0.89% ± 0.32%	0.81% ± 0.27%	1.10 ± 0.55
PDS 66	0.33% ± 0.11%	0.26% ± 0.06%	1.29 ± 0.52
V4046 Sgr	0.46% ± 0.18%	0.55% ± 0.12%	0.85 ± 0.37
DoAr 44	0.55% ± 0.20%	0.65% ± 0.24%	0.85 ± 0.45
AS 209	0.18% ± 0.07%	0.18% ± 0.04%	1.02 ± 0.44

$A_v = 1.2$ (see Table 5). However, our (conservative; see below) error estimates are large for these colors, such that essentially all disk colors agree with each other within the error bars. This evidence, just like the fact that all other disks except for PDS 66 are red, thus remains circumstantial.

It is important to keep in mind that the correction for self-cancellation we employ is a new technique and depends on the quality of the PSF used. PSF fluctuations can thus cause over- or undercorrection of the polarized flux, especially close to the coronagraph edge, potentially introducing errors. We are not able to estimate the quality of the PSF used for correction (which comes from the flux frames) compared to the mean PSF during the science observations in a meaningful way. We construct error bars by measuring the reflected light in both the uncorrected and corrected frames and assume our errors to be smaller than the difference of the two measurements. This is a conservative error estimate, even though it does not take into account errors from, e.g., the flux measurement of the star, as we expect those errors to be negligible compared to the effect the correction for self-cancellation has.

We also look at azimuthally averaged surface brightness curves (Figure 3). Again, we are aware that this does not take into account the inclination of the disk. In this case, we have to correct for the distance, because while the surface brightness is independent of distance, the stellar flux is not. We thus normalize the brightness of the disk (in mag arcsec^{-2}) with the magnitude of the star (as seen from 100 pc). Given the fact that we do only relative comparisons, we do not need to perform an absolute flux calibration of our data. The S/Ns for these surface brightnesses are determined from the variance in the U_ϕ images (see the Appendix for a detailed description) and are shown separately in the bottom panel. We do not take errors that apply equally to all data points, such as errors in the flux measurement or distances to the stars, into account. For comparison, we also calculated the S/N from the variance in

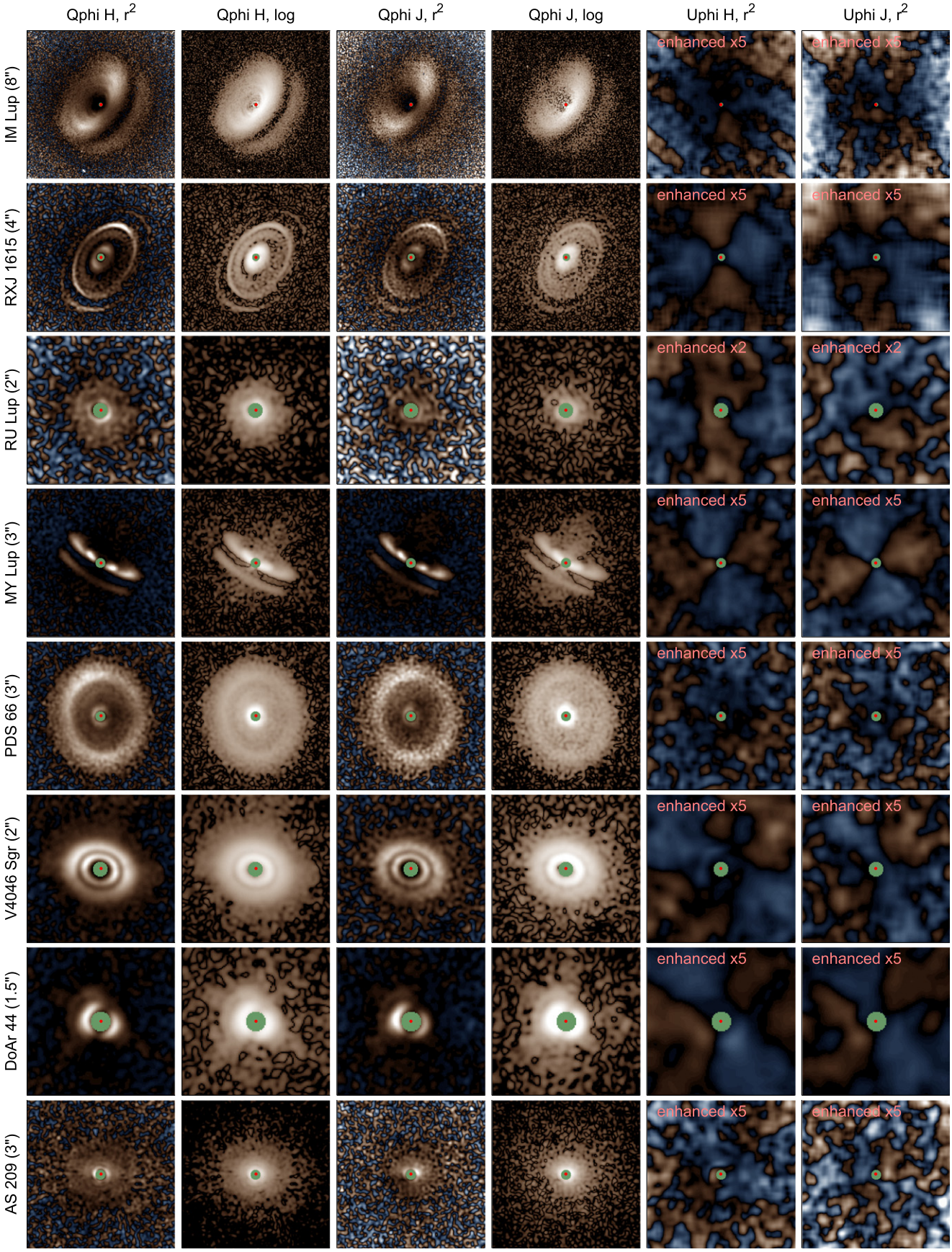

Figure 2. All of our observations, corrected for self-cancellation as described in the Appendix and reconvolved with a 75 mas FWHM Gaussian. The horizontal/vertical FOV is given with the name of the disk. Blue hues correspond to negative values, brown hues to positive values. North is up and east is to the left in all frames.

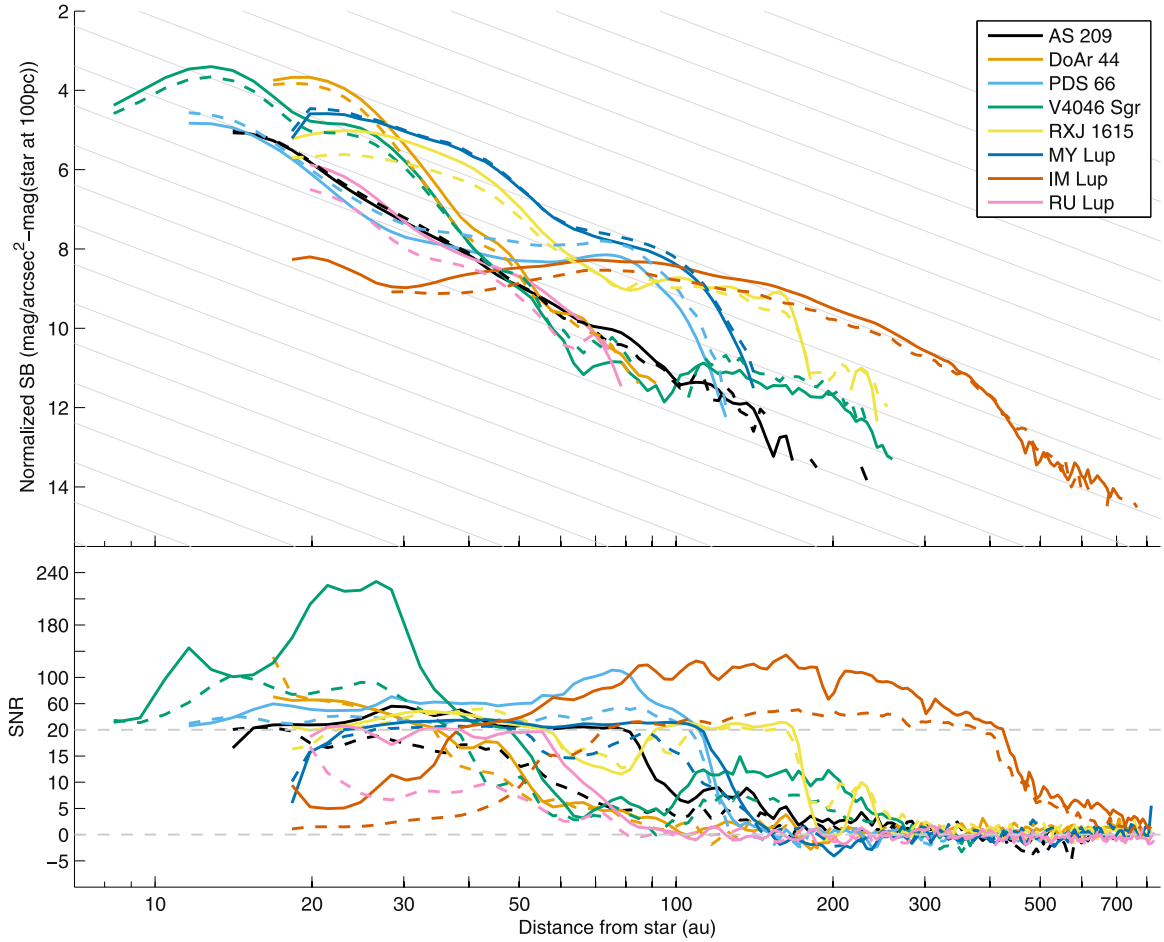

Figure 3. Upper panel: azimuthally averaged, normalized surface brightness vs. distance from the host star for our targets, derived from the self-cancel-corrected images reconvolved with a 75 mas Gaussian. Solid lines represent *H*-band and dashed lines *J*-band data. The width of the annuli used for averaging increases with radius proportional to $r^{1/2}$ (at 50 au, we use a width of 2.5 au). For the sake of readability, error bars are omitted, and data are only shown where the detection is $>3\sigma$ or the combined detection in the *J* and *H* bands is $>3\sigma$ and the detection in the individual band is $>2\sigma$. The lower panel shows the S/N for all of the data, with noise estimated from the U_ϕ frames. Note the change in scale at S/N = 20. Also note that even for our weakest detection, RU Lup, the S/N peaks at $>25\sigma$. The significant negative S/N excursion at ≈500–600 au for AS 209 is to be discarded; it stems from time-variable striping of the IRDIS detector. The gray background lines are for guiding the eye and scale as r^{-2} (similar to the drop-off of stellar light with distance). Note that errors or changes in the distance to the star, especially for those without *Gaia* measurements, would shift the curves along these background lines. Surface brightness plots in observational units, including the surface brightnesses of the U_ϕ frames, can be found in Figure 11.

the Q_ϕ (rather than U_ϕ) images. The maximum S/N determined in this way is significantly lower (≈35) due to azimuthal flux variations in the Q_ϕ frames, but this effect is very much negligible in low-S/N regions, where there is not much flux to begin with. Thus, the regions where disk flux is detected at significant levels are virtually identical. Far out, the signal drops below the detection threshold for all disks, though this point is at ≈700–800 au for IM Lup, which makes it by far the most extended disk in our sample.

4.2. Ring and Spiral Structures

Several of our disks show ring structures (best seen in Figure 2). In RXJ 1615, MY Lup, PDS 66, and V4046 Sgr, full rings are seen, while DoAr 44 potentially shows a broken ring, resembling a smaller version of the HD 142527 disk (Avenhaus et al. 2014b, 2017), very close to the coronagraph edge (discussed in more detail in Casassus et al. (2018). IM Lup shows several substructures in the *H*-band image that, at first sight, are hard to classify as either rings or a tightly wound spiral. In the *J*-band images, these substructures are washed out due to the lower Strehl.

In order to investigate the rings in our data, we employ a method to automatically trace and fit the rings. In a first step, we deproject the data in order to be able to scale them by r^2, accounting for the drop-off of stellar illumination with distance. We then trace the ring at equally spaced position angles by fitting a fourth-order polynomial to the surface brightness in the radial direction using a Markov chain Monte Carlo (MCMC) code in order to be able to determine the error in the position of the peak flux and reproject the fitted points into the image space. We use a second MCMC in order to fit the radius, inclination, position angle, and *h/r* (i.e., the vertical offset off the midplane) of the ring. We assume the eccentricity of the rings to be zero. Because want to fit the ring in r^2-scaled surface brightness, we need to know the parameters of the ring in order to deproject for the first step of our routine. Thus, we start with an estimate for the parameters and iterate until convergence on a final solution is achieved. This allows us to also test the stability of our solution. The MCMC gives us access to statistical error bars for our parameters.

We do perform a number of checks to validate our results. First, we check whether it makes a difference whether we use a

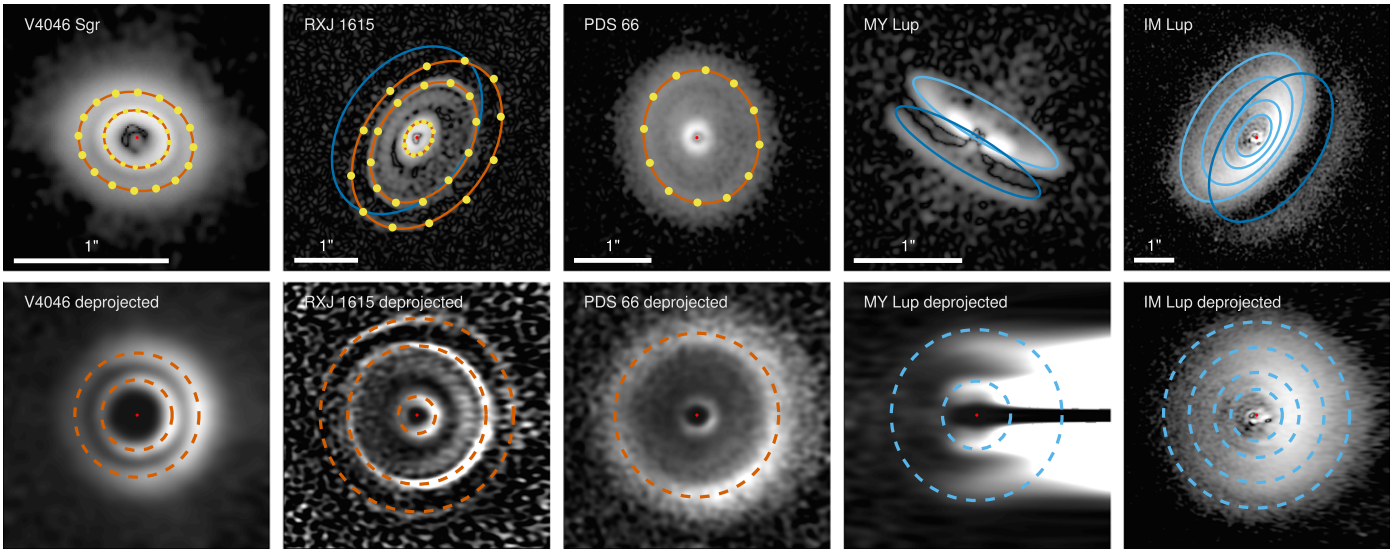

Figure 4. Upper row: disks of V4046 Sgr, RXJ 1615, and PDS 66 overlaid with their ring fits. For MY Lup and IM Lup, rings were overlaid by eye, because the automatic fitting procedure failed. Tracking points are yellow, ring fits are red, and rings overlaid by eye are light blue. The rear edge of the disk (mirrored from the outermost ring) is shown in dark blue where applicable (MY Lup, IM Lup, RXJ 1615). Lower row: deprojected images of the disks overlaid with their rings. We use flaring exponents of $\alpha = 1.605$ (V4046 Sgr), 1.116 (RXJ 1615), and 1.271 (IM Lup) for deprojection (see Section 4.3). For MY Lup and PDS 66, where only one ring can be tracked, we use $\alpha = 1.2$. In the deprojected image of MY Lup, we additionally mark the approximate position of the second ring further in at $r = 0\farcs31/49$ au. For the deprojections, the semimajor axis is along the vertical, the semiminor axis is along the horizontal, and the near side of the disk is always on the right. For the non-deprojected images, north is up and east is to the left.

Table 4
Ring Fits

Ring	Radius (arcsec)	Radius (au)	Inclination	Pos. Angle	Flaring (h/r)
V4046 Sgr ring 1	0.212 ± 0.001	15.35 ± 0.06	30.°53 ± 0.°62	74.°40 ± 1.°04	0.093 ± 0.006
V4046 Sgr ring 2	0.373 ± 0.001	27.01 ± 0.10	32.°18 ± 0.°51	74.°66 ± 0.°72	0.130 ± 0.004
RXJ 1615 ring 1	0.279 ± 0.002	44.00 ± 0.26	43.°90 ± 1.°12	150.°61 ± 0.°94	0.148 ± 0.018
RXJ 1615 ring 2	1.040 ± 0.003	164.00 ± 0.54	47.°16 ± 0.°87	145.°04 ± 0.°48	0.168 ± 0.012
RXJ 1615 ring 3	1.455 ± 0.013	229.44 ± 1.99	46.°78 ± 1.°50	143.°82 ± 1.°74	0.183 ± 0.020
PDS 66 ring 1	0.861 ± 0.004	85.12 ± 0.34	30.°26 ± 0.°88	189.°19 ± 1.°33	0.139 ± 0.012
MY Lup ring 1 (*)	0.77 ± 0.03	120.57 ± 4.70	77° ± 1.°5	239° ± 1.°5	0.21 ± 0.03
IM Lup ring 1 (*)	0.58 ± 0.02	91.90 ± 3.17	53° ± 5°	325° ± 3°	0.18 ± 0.03
IM Lup ring 2 (*)	0.96 ± 0.03	152.11 ± 4.75	55° ± 5°	325° ± 3°	0.18 ± 0.04
IM Lup ring 3 (*)	1.52 ± 0.03	240.84 ± 4.75	55° ± 5°	325° ± 3°	0.23 ± 0.04
IM Lup ring 4 (*)	2.10 ± 0.08	332.75 ± 12.68	56° ± 2°	325° ± 2°	0.25 ± 0.05

Note. Results from fitting the rings present in our data. It is assumed that the rings are circular and displaced in the vertical direction from the disk midplane. Note that this means that the h/r parameter describes the height of the ring over the disk midplane divided by the radius of the ring. This does not correspond directly to the gas scale height of the disk, which we cannot measure with our data, but rather the height of the last scattering surface. Note that the rings of IM Lup and MY Lup (marked with $*$) are not fit using our procedure but by eye. The radii in au are calculated using the distances to the stars and do not take into account the uncertainties in these distances, only the statistical errors from the MCMC.

fourth- or third-order polynomial to fit the position of the peak fluxes. Second, we visually check whether the fits of our rings coincide well with the location of the rings in the image (see Figure 4). Third, we start from a variety of initial guesses for the parameters and check whether we converge to the same solution (which is the case). We also check whether it makes a difference at how many azimuthal points we trace the ring (we tried using 8, 12, 16, 24, and 32 points, settling on 12 points for PDS 66 and RXJ 1615 and 16 points for V4046 Sgr, because convergence was reached fastest for these values).

For both V4046 Sgr and PDS 66, the ring fits are stable and agree within their error bars, independent of the number of fitting points or polynomial order used. For these two disks, we use the images corrected for self-cancellation of the disk (convolved with a 75 mas FWHM Gaussian). The main difference in using these images compared to the uncorrected images is that the rings appear to be at smaller radii, specifically, the rings close to the coronagraph edge (which makes sense given that the innermost regions are most affected by the self-cancellation). This effect is very minor, though (<5%). The rings of RXJ 1615 are significantly more difficult to fit, and convergence is not reached for all numbers of tracking points. Also, using the corrected images makes the fits behave erratically, and we thus choose to use the uncorrected data instead, where our method converges better. The problems mainly affect the h/r of the fit, which is unsurprising given the low S/N of the disk along the semiminor axis. Asymmetries within the disk (see below) might also play a role.

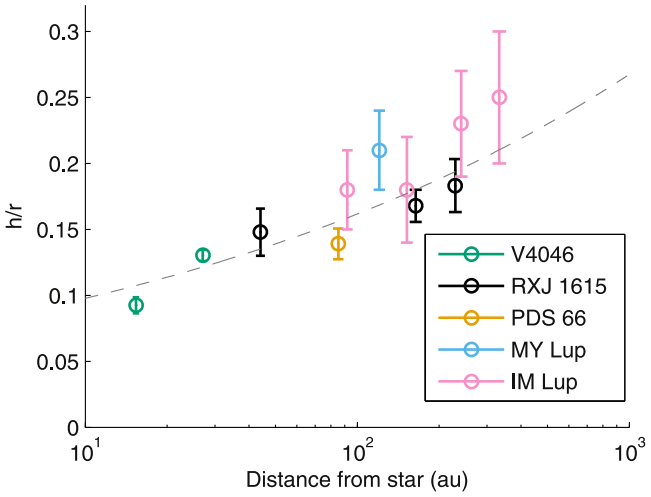

Figure 5. Measurement of the *h/r* parameter of the rings we fit plotted against the distance from the star. There is a clear trend toward higher *h/r* with larger distance. In fact, a single fit to all measurements yields $\alpha = 1.219$ and *h/r* (100 au) = 0.1617 (gray dashed line). This fit is mostly meant to guide the eye but works reasonably well for all disks except V4046 Sgr, which, if considered separately, has a significantly higher flaring parameter.

We are able to fit three rings for RXJ 1615, two rings for V4046 Sgr, and the outer ring of PDS 66. RXJ 1615 clearly shows another ring between the first and second ring we track, but it is only seen on the northeastern side, and we do not attempt to fit it. The broken ring of DoAr 44 is too close to the coronagraph for fitting to yield reliable results. The rings of MY Lup are too inclined to allow for automated tracking of the entire ring at all position angles, and the outer ring/edge of the disk of IM Lup is so wide and diffuse that automatic tracking fails. We do, however, manually (by eye) overlay rings on these two disks to get approximate estimates for their parameters.

For our fits, we assume the rings to be perfectly circular; i.e., they are not displaced from the center and thus have an eccentricity of zero. We do not fit an offset of the ellipse from the stellar location, but the offset is intrinsically defined by the parameters we fit as

$$o_c = R_{\rm ring}\left(\frac{h}{r}\right)\sin(i)$$

in the direction of P.A. + 90°. While it is possible that the rings have an eccentricity or are not centered on the star, we do not find strong evidence for this. The rings are largely compatible with the errors of the fitted ring points, especially in the direction of the semimajor axis. The possible exception is the rings of RXJ 1615 (discussed below), but our data are of too low S/N to reliably fit two additional parameters (eccentricity and position angle for the eccentricity), especially since these would be highly correlated with the inclination and *h/r* in our fits.

Our results are shown in Table 4 and Figure 4. For the rings where fitting is possible, the errors quoted are 1σ errors from the MCMC fit. For the ones fit by eye, they are meant to represent approximate errors obtained by varying the parameters and seeing when they clearly do not fit any longer. There is no strong correlation between any of the variables except for the inclination and *h/r*, which are moderately correlated.

Our ring fits are overlaid on the images in Figure 4, where we also show deprojected versions of our disks. For V4046 Sgr and PDS 66, there is no evidence for any asymmetries (such as breaks or deviations from circular structure) in the rings. RXJ 1615, on the other hand, shows some weak asymmetries, specifically in the second ring toward the southwest (upper left in the deprojected image), where the structure of the otherwise circular ring appears to be broken. This might be part of the reason for the fit being less stable than that for the other disks. Furthermore, it is interesting that the theoretical rear edge of the disk (from mirroring the outermost ring to the back side) does not coincide with the faint ring arc that is seen toward the northeast of the disk. This might be because the actual disk is slightly larger than the outermost ring seen. A similar effect is seen in IM Lup (toward the southwest).

Not surprisingly, the quality of the deprojections is lower for highly inclined disks, especially for MY Lup, where the near side of the disk goes through the position of the star. However, deprojection still makes it possible to more clearly see the location of the second ring. What is also clear is that our naive visual fitting of the rings does not produce the correct radii of the ring, but rather fits the position of the outer edge.

4.3. Vertical Disk Structures

When looking at more than one ring, the behavior of *h/r* with radius can be described as a power law,

$$\frac{h}{r} = \frac{h_0}{r_0}\cdot\left(\frac{r}{r_0}\right)^{(\alpha-1)},$$

where h_0 describes the h/r value at a radius r_0, and α is the flaring index. Here α has to be higher than 1 in order to see the outer rings, because otherwise they would lie in the shadow of the inner rings. This also means that h/r should be increasing with radius. We show all h/r values we measure in Figure 5, where it can be seen that h/r clearly does increase with radius.

Theoretical studies can derive flaring indices based on assumptions about the disk physics and geometry. For example, the Chiang & Goldreich (1997) model, by assuming a surface density profile $\sigma(r) \propto r^{-1.5}$, gives a temperature profile that translates into a maximum flaring index of $\alpha = \frac{9}{7} \approx 1.29$. For a thin disk model with very small mass compared to the central star, the flaring is expected to be $\alpha = \frac{9}{8} = 1.125$ by Kenyon & Hartmann (1987). The same authors derived the maximum flaring angle to be $\alpha = \frac{5}{4} = 1.25$.

In practice, we measure a flaring index of 1.605 ± 0.132 in the case of V4046 Sgr, 1.116 ± 0.095 in the case of RXJ 1615, and 1.271 ± 0.197 for IM Lup. These values (and errors) are acquired by fitting a power law to the *h/r* measurements of the rings and are only possible for disks where more than one ring can be measured. V4046 Sgr seems to be the clear outlier here, with a significantly higher flaring index, inconsistent with the aforementioned theoretical values. This is surprising given the fact that it is the oldest disk in our sample (and disks tend to settle with age). The flaring of this disk could potentially be affected by the fact that V4046 Sgr is a K-dwarf spectroscopic equal-mass binary. V4046 Sgr is also special in the sense that the rings we fit here are by far the closest to the star and it has a wide-separation binary companion (Kastner et al. 2011).

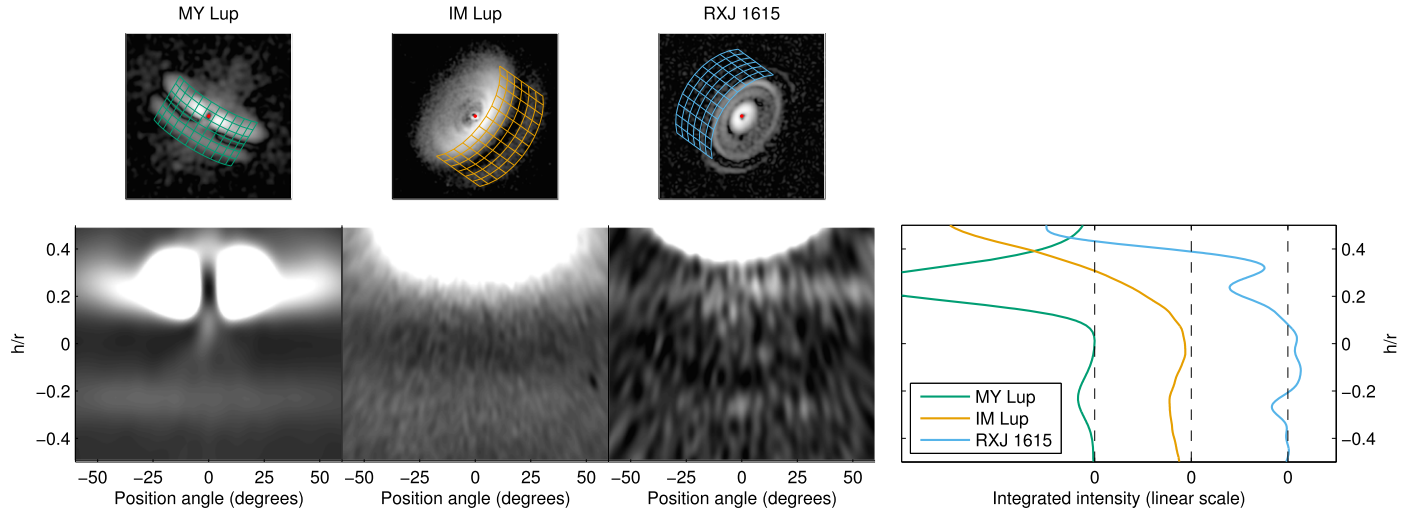

Figure 6. Left: deprojection of the disk rims and surface brightness profiles perpendicular to the disk rim of MY Lup, IM Lup, and RXJ 1615, shown in linear scale. The position angle refers to the position angle with regard to the disk minor axis. The meshes in the upper panels give a reference to show how the deprojection was done. Right: integrated intensities along the disk plane between −60° and +60°. The scaling of the data for the different disks with respect to each other is arbitrary. As can be seen, the surface brightness goes into the negative for RXJ 1615, a sign that we overcorrected for self-cancellation.

Table 5
Derived Properties for Our Targets

Target	$T_{\rm eff}$ (K)	$A_{\rm v}$ (mag)	Age (Myr)	$M_\star$ ($M_\odot$)	$L_\star$ ($L_\odot$)	$M_{\rm dust}$ ($M_\oplus$)	$f_{\rm NIR}/f_\star$ (%)	$f_{\rm FIR}/f_\star$ (%)
IM Lup	4000	0.5	1.1 ± 0.2	0.7 ± 0.1	1.56 ± 0.05	121 ± 13	3 ± 1	8 ± 1
RXJ 1615	4400	0.6	4.5 ± 2.1	0.8 ± 0.1	0.99 ± 0.03	72 ± 4	0 ± 1	9 ± 1
RU Lup	4000	0.0	1.2 ± 0.4	0.7 ± 0.2	1.44 ± 0.13	95 ± 6	40 ± 4	30 ± 2
MY Lup	5200	1.2	12.7 ± 4.4	1.3 ± 0.1	1.35 ± 0.07	27 ± 3	3 ± 1	8 ± 1
PDS 66	5000	0.8	11.7 ± 3.3	1.4 ± 0.1	1.36 ± 0.11	43 ± 3	7 ± 1	7 ± 1
V4046 Sgr	4400	0.0	10.0 ± 3.8	1.1 ± 0.1/0.7 ± 0.1	0.36 ± 0.05/0.27 ± 0.04	37 ± 5	1 ± 1	9 ± 1
DoAr 44	4800	2.2	6.8 ± 2.4	1.5 ± 0.1	1.88 ± 0.17	39 ± 5	11 ± 2	9 ± 1
AS 209	4600	0.8	1.9 ± 0.9	1.1 ± 0.1	1.75 ± 0.07	78 ± 8	7 ± 2	19 ± 2

Note. Rederived properties of our target stars and disks from our stellar modeling. The effective stellar temperature is based on the spectral type of the star (cf. Cohen & Kuhi 1979), while the extinctions are calculated from the SIMBAD colors and cross-checked with literature values. The relevant spectral types and distances can be found in Table 1. The errors for the 1.3 mm fluxes (also found in Table 1) are typically small (∼5%). For the visual extinction, we assume an error of 0.2 mag. Note that V4046 Sgr is a binary, which we assume to be coeval. Further descriptions of our derivations can be found in the main text.

If we use all data to fit the flaring behavior of our disks, we arrive at $\alpha = 1.219 \pm 0.026$ and $h/r(100\,\mathrm{au}) = 0.1617 \pm 0.0051$ (see Figure 5). While this is in reasonable agreement with theoretical studies (Kenyon & Hartmann 1987; Chiang & Goldreich 1997), it is difficult to interpret given the fact that all of our systems are different and have no physical connection, and thus also no reason to show the same flaring, unless there is some intrinsic physical process that drives all disks toward a similar flaring behavior. We also have to remember that we can only measure the flaring of the last scattering surface using scattered-light data and do not measure the flaring of the gas scale height directly.

4.4. Disk Rims and Midplane Shadows

For three of our disks (IM Lup, RXJ 1615, and MY Lup), the outer edge of the disk and thus the lower disk surface can be seen. To illustrate this, we deproject the *H*-band images of these outer rims for position angles from −60° to +60° around the disk minor axis. The resulting deprojections can be seen in Figure 6. These deprojections use the data after correction for systematic self-cancellation and reconvolution with a Gaussian kernel (see the Appendix). We use a 100 mas FWHM kernel here in order to achieve slightly better smoothing for these faint features.

The deprojection shows that the two disk sides are parallel in all cases. However, it is not possible to estimate how dark the midplanes actually are. Without the discussed correction, the PSF convolution smears light from the disk upper and lower sides into the visible midplane gap. With correction, we can see that the midplane runs into negative values for RXJ 1615 (in fact, it partially does so for MY Lup as well). This is a sign of an overcorrection due to the application of a PSF that is worse than the average PSF encountered during the observations (this will be discussed in H. Avenhaus et al. 2018, in preparation).

What can be seen, however, is that the two bright lanes on the disk rim of IM Lup are relatively broad, significantly broader than the 100 mas kernel the data has been (re)convolved with. For both MY Lup and RXJ 1615, these features are much narrower (one has to remember that for MY Lup, they are much closer to the star, thus the same *h/r* range is a smaller physical scale). This could mean that for IM Lup, the disk at the location of the outer rim is optically thinner, allowing for deeper penetration of the stellar light and thus a larger range in heights above the midplane where light is scattered.

5. Discussion

5.1. Ages and Stellar/Dust Disk Masses

To place our data set in context, we self-consistently calculate several stellar and disk properties. For all of our targets, Gaia DR2 distances are available, which makes a recalculation of the stellar ages particularly worthwile. To be consistent, we rederive the properties for all sources in our sample. To do so, we retrieved the visible–to–far-IR photometry for each source from SIMBAD and assumed a PHOENIX model of the stellar photosphere (Hauschildt et al. 1999) with solar metallicity, $\log(g) = -4.0$, and effective temperature $T_{\rm eff}$ obtained from the spectral type of the star (found in Table 1). We use the relation described in Cohen & Kuhi (1979). The choice of $\log(g)$ is not critical, as within a range of reasonable values, its impact on the stellar luminosity is marginal. Furthermore, we found self-consistency with the values of stellar mass and radius constrained at the end of this analysis. We dereddened the observed photometry by means of the optical extinction $A_{\rm V}$ available from the literature and scaled the photospheric model to the dereddened magnitude in the J band. We then integrated the photospheric flux and converted it into the stellar luminosity L_* using the distances found in Table 1. Uncertainties on these estimates are primarily from $A_{\rm V}$. We considered a $\Delta A_{\rm V} = 0.2$ and a 5% error for the 1.3 mm photometry, as well as the error from the *Gaia* distance and then propagated these uncertainties. Errors on $T_{\rm eff}$ are negligible in our error budget. Using the pre-main-sequence tracks by Siess et al. (2000), we constrained the stellar age and mass as shown in Table 5. We take into account the fact that V4046 Sgr is a spectroscopic binary, but assume the two stars to be coeval and distribute the flux between them based on their spectral types (K5 and K7). More detailed derivations of the parameters for this particular system can be found (e.g. Donati et al. 2011; Kastner et al. 2011; Rosenfeld et al. 2012), but for reasons of consistency, we use the values we derive using our simplified approach for our comparisons.

We also calculated the near- and far-IR excess of our sources similarly to Garufi et al. (2017b). These values were found by integrating the flux exceeding the stellar photosphere from 1 to 5 μm and 20 to 400 μm, respectively. The relative uncertainties are given by the aforementioned uncertainty on $A_{\rm V}$.

Finally, we refined the estimate of the disk dust mass. To do so, we recovered the flux at 1.3 mm for all sources and scaled it as in Beckwith et al. (1990) under the assumption that this emission is optically thin and by assuming a typical dust opacity of 2.3 $\rm cm^2\,g^{-1}$ (e.g., Andrews & Williams 2005) and a disk temperature of 25 $L_*/L_\odot$ K (as in Andrews et al. 2013), where L_* is what we obtained above. The results are also shown in Table 5.

By comparing the obtained stellar ages and disk dust masses relative to their host star masses, we obtain the diagram found in Figure 7. While the error bars are large, the trend clearly points toward lower dust (disk) masses at advanced ages (as is to be expected). The three very young stars in our sample host a massive disk (in dust). This is somewhat surprising—while the fact that the disk of IM Lup is young and massive can be expected just from looking at our scattered-light data, the other two very young sources (RU Lup and AS 209) appear faint, compact, and featureless in scattered light. At the same time, our calculations based on their 1.3 mm fluxes show that their disks must be massive. While stellar age and dust mass seem correlated, there is no correlation between either parameter and disk substructure or total reflected light to be seen. However, it is worth pointing out that the two targets with faint disks (RU Lup and AS 209) at the same time have the highest accretion rates among our sample (cf. Table 1).

Table 6
Comparison of Ring Fits for RXJ 1615

#	Par.	This Work	ADI-H23	PDI-J
1	R [arcsec]	0.279 ± 0.002	0.30 ± 0.01	0.35 ± 0.01
	incl. [deg]	43.9 ± 1.1	49.0 ± 3.9	47.7 ± 4.1
	PA [deg]	150.6 ± 0.9	145.4 ± 4.2	144.5 ± 4.3
	h/r	0.148 ± 0.018	n/a	n/a
2	R [arcsec]	1.040 ± 0.003	1.06 ± 0.01	1.06 ± 0.01
	incl. [deg]	47.2 ± 0.9	48.5 ± 1.3	46.8 ± 1.4
	PA [deg]	145.0 ± 0.5	145.4 ± 1.3	144.3 ± 1.4
	h/r	0.168 ± 0.012	0.158 ± 0.014	0.152 ± 0.013
3	R [arcsec]	1.455 ± 0.013	1.50 ± 0.01	1.50 ± 0.01
	incl. [deg]	46.8 ± 1.5	47.3 ± 1.0	47.0 ± 0.8
	PA [deg]	143.8 ± 1.7	145.7 ± 1.0	144.2 ± 0.8
	h/r	0.183 ± 0.020	0.162 ± 0.009	0.162 ± 0.007

Note. Comparison between the ring parameters derived in this work and those derived by de Boer et al. (2016) using H-band ADI (column ADI-H23) and J-band PDI (column PDI-J).

Both also show very different SEDs from the rest of the sample. Their IR excess is in fact much more prominent (19% and 30% of the stellar flux) than that of the other objects (∼7%–9%). In other words, a large amount of thermal reprocessing of the stellar light occurs around AS 209 and RU Lup, and their dusty material is, along with that of IM Lup and RXJ 1615, the most abundant among the sources of this work. RU Lup also has the highest near-IR excess at 40%, hinting at significant amounts of material close to the star.

The solution to this apparent incongruity is not obvious, but it is possible that the scarcity of detectable scattered light from the disk is related to a self-shadowing effect. This is the most likely explanation for the so-called Group II disks around Herbig Ae/Be stars, where the absence of a large disk cavity prevents the stellar light from reaching the outer disk regions (see, e.g., Garufi et al. 2017b). Since we cannot probe the disk at separations of less than ∼100 mas, a lot of scattered light could be hidden in these innermost regions. In both disks, the disk extends down to the coronagraph, and no inner hole is detected. This is consistent with the literature, which shows that both disks extend close to the star (Takami et al. 2003; Fedele et al. 2017). However, the classifying criterion for Group II sources in the case of Herbig stars is the low far-IR excess (Meeus et al. 2001), which is the opposite trend to that of AS 209 and RU Lup. Furthermore, Herbig Group II stars are relatively old (>3 Myr), and their observations in PDI typically reveal either a compact but strong signal close to the star (<30 au) or nothing at all, whereas our data for AS 209 and RU Lup show a relatively extended and faint signal.

We are thus more inclined to believe that the PDI data of AS 209 and RU Lup reflect a geometry similar to that of RY Tau, which is another young T Tauri star with a prominent IR excess but a relatively faint, diffuse, and featureless signal in PDI (Takami et al. 2013). According to these authors, this source would (still) be surrounded by optically thin and geometrically thick uplifted material that is entirely responsible for the observed scattered light and partly for the IR excess,

whereas the underneath thin disk would only contribute to part of the IR excess. This explanation may hold for these two sources as well and would also explain the absence (RU Lup) or faintness (AS 209; cf. Section 5.2.8) of disk features from our images in a framework where all PDI images of protoplanetary disks with sufficient S/N available from the literature show some sort of substructures—except, to our knowledge, RY Tau.

5.2. Individual Targets

5.2.1. IM Lup

Our results for IM Lup are most readily compared to those derived by Pinte et al. (2008). These authors imaged the disk of IM Lup with the *HST* in the visible and near-IR. Their results in terms of disk position angle are consistent with our results: 143° ± 5° (compared to our estimate of 325/145° ± 2°). They are also able to detect the lower surface of the disk, as well as the dark lane between the two disk surfaces, results that we can confirm at much higher S/N. Our results additionally allow us to detect substructure in the disk upper surface, although it is not entirely clear whether this substructure represents rings or tightly wound spiral structures. We are also able to trace the disk to much smaller angular separations. Pinte et al. (2008) described a faint halo out to ≈4.″4, which they ascribed to a tentative optically thin envelope around the disk. In our surface brightness profile (Figure 3), it can be seen that while the azimuthally averaged surface brightness drops steeply beyond 400–450 au (2.″5–2.″8), the signal can be detected out to >700 au (4.″4). The signal in this region is very faint and cannot be seen directly in the images, but only when azimuthally averaging. It is also relatively close to the edge of the detector, where various imperfections occur. However, none of the other sources show a consistent signal in both the *J* and *H* bands at these angular separations; thus, we conclude that this signal is indeed real. However, the faint envelope must be optically thin, given that the back side of the disk can be seen through it.

The disk is modeled with a gas pressure scale height of 10 au at a radius of 100 au with a flaring index of 1.13–1.17 by Pinte et al. (2008; $h/r = 0.1$). This can be compared to our estimate of $h/r = 0.18 \pm 0.03$ at a similar radius (see Table 4), which suggests that the $\tau = 1$ scattering surface resides at around 1.8 pressure scale heights. Our estimate for the flaring index is much less well constrained at 1.27 ± 0.20 (also remember that the fitting was done by eye) but consistent with these results.

Panić et al. (2009) described the Submillimeter Array (SMA) data of the source, with which they were able to determine Keplerian rotation of the disk in the clockwise direction (as seen from our vantage point). They furthermore constrained the disk inclination to 54° ± 3°, consistent with our estimate of 56° ± 2° for the outermost ring. The disk can be traced in the gas out to 900 au (assuming a distance of 190 pc, translating to 751 au at the *Gaia* distance of 158.45 pc, similar in radius to our scattered-light observations), while the continuum observations can trace the dust only to around 400 au (334 au given the updated distance). Their model thus requires a break in the disk surface density at around this distance, which is consistent with the scattered-light observations, which show that the disk is truncated relatively sharply beyond 400 au (2.″5), with the outermost ring we trace at 2.″1 ± 0.″08 (333 ± 13 au).

More recently, two tentative dust rings have been detected at millimeter wavelengths by ALMA (Cleeves et al. 2016; Pinte et al. 2017), with radii of ≈150 and ≈250 au, i.e., approximately where we observe the faint rings 2 and 3 in our *H*-band image. The current resolution of the ALMA observations of IM Lup (≈0.″3) is insufficient to determine if there is any structure at millimeter wavelengths that could be associated with our ring 1. The millimeter emission drops sharply outside of 310 au, and no emission is detected at the location of our ring 4.

Pinte et al. (2017) used the individual channel maps of the CO isotopologues to determine the altitude of the emitting layers. Interestingly, the scattered-light $\tau = 1$ surface we measure ($h/r \approx 0.2$ around 200 au) appears to be located between ^{13}CO ($h/r \approx 0.16$) and ^{12}CO ($h/r \approx 0.35$) at the same radii. No evidence of structure has been detected in the CO map, possibly due to the limited spatial resolution of the observations (≈0.″3). Observations of the CO emission at higher spatial resolution could potentially detect the counterpart of the structures we see in the SPHERE data and shed some light on their nature, in particular their kinematics.

5.2.2. RXJ 1615

The disk of RXJ 1615 was previously detected and described by de Boer et al. (2016) using both SPHERE/IRDIS H2H3 dual-band angular differential imaging (ADI) and IRDIS *J*-band and ZIMPOL *R*-band PDI. They clearly detected rings 2 and 3 that we describe (which they called R2 and R1, respectively), along with an arc inside of those two rings (A2), which we describe here as well. This arc is most likely a full ring, which we are able to trace for more than 180° (see Figure 6 and discussion in Section 4.2). They described an elliptical inner disk component, which we fit here as our ring 1.

They also described an arc outside the outermost ring and discussed whether it is another ring or the back side of the disk. Given our higher-S/N polarimetric observations, we are convinced that this is indeed the disk back surface, even though it is not at the location of the projected outermost ring of the front surface of the disk. This can be explained by the fact that (a) the light has to "bend around" the disk edge to reach us from the disk back surface, and (b) the truncation radius of the disk must not necessarily coincide with the radius of the outermost surface ring (ring 3 in our discussion). Besides the fact that the geometrical structure in our images and deprojections (see Figure 6), as well as the data shown in de Boer et al. (2016), seem more consistent with this geometry, we would expect a fourth ring to be most easily detected along the disk major axis (where the S/N for all other rings is highest) rather than the disk minor axis. We thus strongly favor the back surface explanation over the additional ring.

De Boer et al. (2016) also fit ellipses to the rings and inner disk. We compare their fits to ours in Table 6. Even though these results do not take into account systematic errors, they agree within the error bars in terms of inclination, position angle, and flaring (*h/r* for the $\tau = 1$ surface). In terms of radii, the results do not agree, but as we pointed out in Section 4.2, the determination of the radii is slightly arbitrary and depends on the exact definition of where you place the peak of the ring.

Our results are also reasonably close to the results from van der Marel et al. (2015), who obtained $i = 45°$ and PA = 153° but did not state errors for these measurements. They modeled the disk with a cavity radius of 17 au, a characteristic radius

(for the exponential taper of the continuum) of 98 au, and an outer radius of 170 au (distances updated using the new Gaia measurement). From our results, we can see that the cavity in small dust grains must be smaller, as we detect scattering down to the coronagraph edge (≈0.″1/15.8 au). We also see that in scattered light, the disk is much larger than 170 au, as the outermost ring is detected at ≈230 au, with the outer edge of the disk likely a bit further out.

5.2.3. RU Lup

RU Lup is the most unremarkable disk in our sample. While the star shares many characteristics with IM Lup (in terms of age, spectral type, submillimeter excess, and SED), the two disks appear completely different in scattered light. RU Lup is both the faintest and reddest disk in our sample (cf. Table 3), though the second measurement could be impacted by bad observing conditions and the fact that both the star and the disk are faint. The disk appears to be brighter in both the *J* and *H* bands in the southwest direction. This could be a hint toward a low-to-moderate inclination along the SE–NW axis, with the SW side being the near side, but this interpretation is speculative (see also the discussion on AS 209 in Section 5.2.8).

RU Lup is known to have a rather high accretion rate of $\sim 10^{-7}\,M_{\odot}\,\mathrm{yr}^{-1}$ (Podio et al. 2007). This could be related to the disk extending very far in and not showing any signs of an inner gap in our scattered-light observations. Archival SPHERE/ZIMPOL data show the disk to extend in to at least ∼40 mas, and Anthonioz et al. (2015) resolved the disk using VLTI/PIONIER and fit it with an inner radius of ∼0.1 au (0.7 mas). ATCA measurements indicate a Gaussian size of the disk of $1.''02 \pm 0.''32$ at 1.4 mm (Lommen et al. 2007), somewhat smaller than the same measurement for IM Lup ($1.''33 \pm 0.''20$).

The most likely explanation for our observations is that the disk of RU Lup is extending very close to the star and is not very flared, such that partial shadowing reduces the amount of light reaching the outer parts of the disk and thus the amount of scattered light to be detected. Whether substructures are present in the disk cannot be determined due to the low S/N.

5.2.4. MY Lup

MY Lup is the most highly inclined disk in our sample but otherwise resembles the structure of the IM Lup and RXJ 1615 disks at smaller size (flared, truncated, with multiple rings on the surface), even though the disk is significantly older than those two targets. Its age has previously been determined to be 16 Myr by Frasca et al. (2017), which is consistent with our estimate of 16 ± 4.3 Myr. However, its spectrum seems to be underluminous compared with young T Tauris with similar spectral types; thus, a younger age is still quite plausible.

This issue is likely related to the high inclination. Because of the disk being so inclined, some of the starlight is obscured by the circumstellar disk. This was previously pointed out by Ansdell et al. (2016) based on their estimate of an inclination of ∼73° and is confirmed by our observations, which clearly show the disk being highly inclined at $\sim 77^{\circ} \pm 1.^{\circ}5$ and indicate obscuration by the outer ring. This also ties in to the disk appearing blue with regard to the starlight, as the starlight is most likely reddened because of being filtered by the dust disk.

5.2.5. PDS 66

Our images confirm the overall morphology of the GPI and *HST* images (Cortes et al. 2009; Schneider et al. 2014; Wolff et al. 2016), with the disk being detected along the major axis out to $1.''25$ (≈124 au) in both the *J* and *H* bands, at which point the signal rapidly drops below the detection limit (cf. Figure 3). This corresponds to the extent of the CO emission (Kastner et al. 2010). The outer ring at $0.''8$ is clearly visible in both wavebands. The northeast and south regions of the ring are the brightest in polarized scattered light (with the former being ≈30% brighter than the latter). This symmetric enhancement at 30° from the disk major axis is most likely entirely due to the maximized polarizing efficiency for a scattering angle of ≈90°, since in disks inclined by ≈30°, this type of scatter roughly occurs at those locations.

The bottom-to-peak contrast between the faint region inside the ring and the ring is, on average, ≈40% in the *H* band (in agreement with the GPI observations in the same waveband) but somewhat higher in the *J* band, i.e., ≈60%. Within the faint region, our images seem to reveal a further discontinuity at a distance of $\approx 0.''6$ (59 au), which is most apparent from the radially scaled image (Figure 2). Finally, the strongest signal is detected from a compact region of $\approx 0.''25$ (25 au) in radius. We do not detect any significant inward decrement of signal close to the coronagraph, ruling out the existence of an inner cavity for μm-sized dust grains larger than ≈10 au.

Wolff et al. (2016) revealed an azimuthal decrease by 35% in polarized light at P.A. = 160°–220° that is persistent across wavebands and that they ascribe to a shadow cast by a density enhancement at the disk inner edge or cold spots on the stellar surface. Our images do not reveal such a dramatic dip in the azimuthal distribution, and neither do the *HST* images, though they are not polarimetric or taken at the same epoch, but they also do not detect variations over two epochs (Schneider et al. 2014). We note at this point that an imperfect correction of interstellar or instrumental polarization will lead to butterfly patterns in the Q_ϕ and U_ϕ images, which, overlaid with the disk image, can make it appear like there are decrements in the disk. We tried to do a very careful job with our correction for interstellar/instrumental polarization (see the Appendix) and do not see any butterfly patterns in the U_ϕ image, indicating that our Q_ϕ data is free of such patterns, too. Looking closely at the Q_ϕ image presented in Wolff et al. (2016), there seems to be a decrement in the other (northern) direction as well, which would be expected for an overlaid butterfly pattern. Unfortunately, these authors do not show their U_ϕ images. We have to also point out, however, that our observations were taken at a different epoch, i.e., almost 2 yr later than the GPI observations.

However, comparing the two bands we have data for, we see a localized dip toward the west (P.A. ∼ 270°) in the *H* band compared to the *J* band. At other azimuths, the two bands are comparable. Given the short baseline of only ≈24 hr between the two observations, this argues for short-term variations, possibly due to shadowing, in the disk or variations in the scale height with wavelength of something that can cast a shadow. The S/N of this feature is low, though, making this detection tentative.

Schneider et al. (2014) described an extended halo outside of the main disk accounting for ∼10% of the total scattered starlight, which we fail to detect in our images (cf. Figures 1 and 2). This could be due to the low S/N we can achieve at

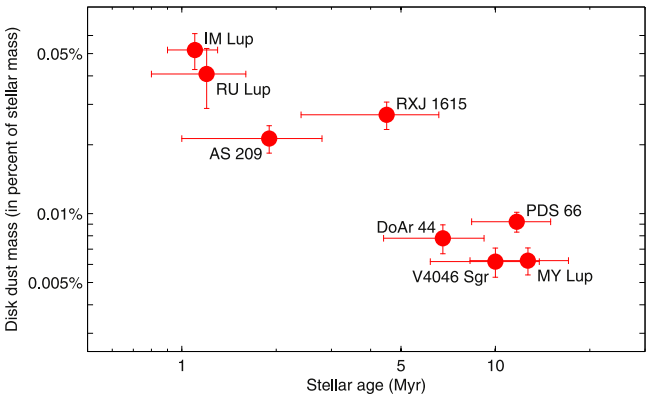

Figure 7. Dust mass relative to stellar mass vs. age of the source, derived from literature data in order to put our data into context. A trend toward lower fractional dust masses with higher ages is visible (as is to be expected). The two disks showing weak signals and no readily visible substructure (RU Lup and AS 209) are, interestingly, among the youngest and most massive disks of our sample.

these large separations and for very faint, optically thin dust, for which *HST* continues to be very competitive (cf. Schneider et al. 2014; Olofsson et al. 2016), even though, given the fact that we detect a halo out to >700 au for IM Lup, this explanation seems unlikely.

5.2.6. V4046 Sgr

V4046 Sgr was previously imaged using GPI, and the results were presented in Rapson et al. (2015a). Our observations confirm their results—a disk with two rings seen in scattered light—at much higher S/N. We cannot, however, confirm their assertion that the scattering efficiency is higher at shorter wavelengths—in fact, the color of the scattering appears to be red, with more light being scattered in the *H* band (cf. Table 3). We also cannot confirm the multiple dark lanes seen in their *J*-band image in the inner ring, though we do see a decrement in the *H*-band image at a P.A. of ∼280°. This feature likely represents shadowing from the second star of the tight binary and will be discussed in more detail in V. d'Orazi et al. (2018, in preparation).

We can confirm through the fitting of rings to the ellipses seen in the image (see Section 4.2) that the northwest side is the near side of the disk. We also see that the far side of the disk appears fainter, characteristic for disks at low-to-medium inclination. This interpretation of the near and far sides of the disk is also consistent with SMA results from Rosenfeld et al. (2012). These authors estimated the inclination of the disk at $33.^{\circ}5^{+0.7}_{-1.4}$. Our estimates are $30.^{\circ}53 \pm 0.^{\circ}62$ for the inner and $32.^{\circ}18 \pm 0.^{\circ}51$ for the outer ring. While this may seem to implicate a trend from smaller to larger inclinations when going from smaller to larger separations and thus a slight warp within the disk, all values agree within 3σ with regard to their respective error bars. Furthermore, the inclination of the central binary system is determined by the same authors, using unpublished radial velocity constraints, to $33.^{\circ}42 \pm 0.^{\circ}01$.

The continuum dust emission of the disk can be fit with a characteristic radius of 45^{+5}_{-3} au, while the CO disk extends out to almost 400 au (Rodriguez et al. 2010; Rosenfeld et al. 2012). This is consistent with the compact, bright, inner regions with the two rings we detect in the scattered light, while an extended halo is seen out to ≈250 au and potentially reaching farther (see Figure 3), much farther than the GPI was able to trace the halo (≈45 au; Rapson et al. 2015a).

5.2.7. DoAr 44

While we do see a bright ring in our DoAr 44 data, with a decrement toward the inside, it is not clear whether this is due to the IRDIS coronagraph or an actual decrement (i.e., gap) in the disk that can be resolved. We know from submillimeter ALMA observations that the gas and dust cavities have radii of 19 and 39 au, respectively (0.″13 and 0.″27; van der Marel et al. 2016), hinting toward dust filtering and an inner edge of the (gas/small μm grains) scattered-light rim indeed very close to the coronagraph edge. The ALMA image also shows a ring at significantly larger separations. In scattered light, the disk surface brightness falls off rapidly beyond the bright inner rim, though scattering can be detected above the noise out to ≈90 au (Figure 3). This again is rather close to the measurements in the submillimeter, where the gas disk can be traced out to ≈70 au, showing that the disk is overall rather small compared to the disks of, e.g., IM Lup and RXJ 1615.

Unfortunately, due to the scattered light being so close to the coronagraph, we are not able to determine an inclination for this disk and are thus not able to confirm the inclination of ≈20° found in van der Marel et al. (2016), though we can confirm that the disk looks to be close to face-on from our observations.

Besides that, the disk resembles a scaled-down version of HD 142527 (Fukagawa et al. 2006; Casassus et al. 2012; Avenhaus et al. 2017), with its bright ring that is broken by two sharp depletions in surface brightness. For HD 142527, these nulls can be explained with an inclined inner disk close to the star, which casts shadows onto the outer disk (Marino et al. 2015). Casassus et al. (2018) consider a similar scenario for DoAr 44.

5.2.8. AS 209

The disk of AS 209 at first sight appears similar to that of RU Lup in that it is relatively faint and small. Tight ringlike substructures that are easily seen in Figure 1 most likely are not of a physical nature, given that they closely resemble the Airy ring pattern of the PSF and are furthermore below the resolution of the beam. This is also shown in Figure 2, where a reconvolution with a 75 mas beam makes these rings disappear, especially in the *J* band (faint structures are still seen in the *H* band).

A possible explanation for these ringlike features at the location of the Airy ring dips is that a bright inner part of the disk, which is known to extend very close to the star (Pérez et al. 2012), is propagated to larger radii through the PSF. The Airy rings of the PSF can dislocate the flux of a bright inner disk well below the resolution of the telescope (for example, around 0.″01 from the star) to larger radii, where constructive interference can occur in the Q_ϕ band. We tested this with a mock-up disk and a perfect Airy ring pattern and were able to produce such rings in Q_ϕ at much larger radii than the location of the disk, consistent with our observations of AS 209. No constructive interference was observed in the U_ϕ band. This can only occur at high Strehl, where Airy rings are observed. This is consistent with the fact that we do not see such effects in RU Lup (where the disk extends in very close as well, though indications for a hole on au scales exist; Takami

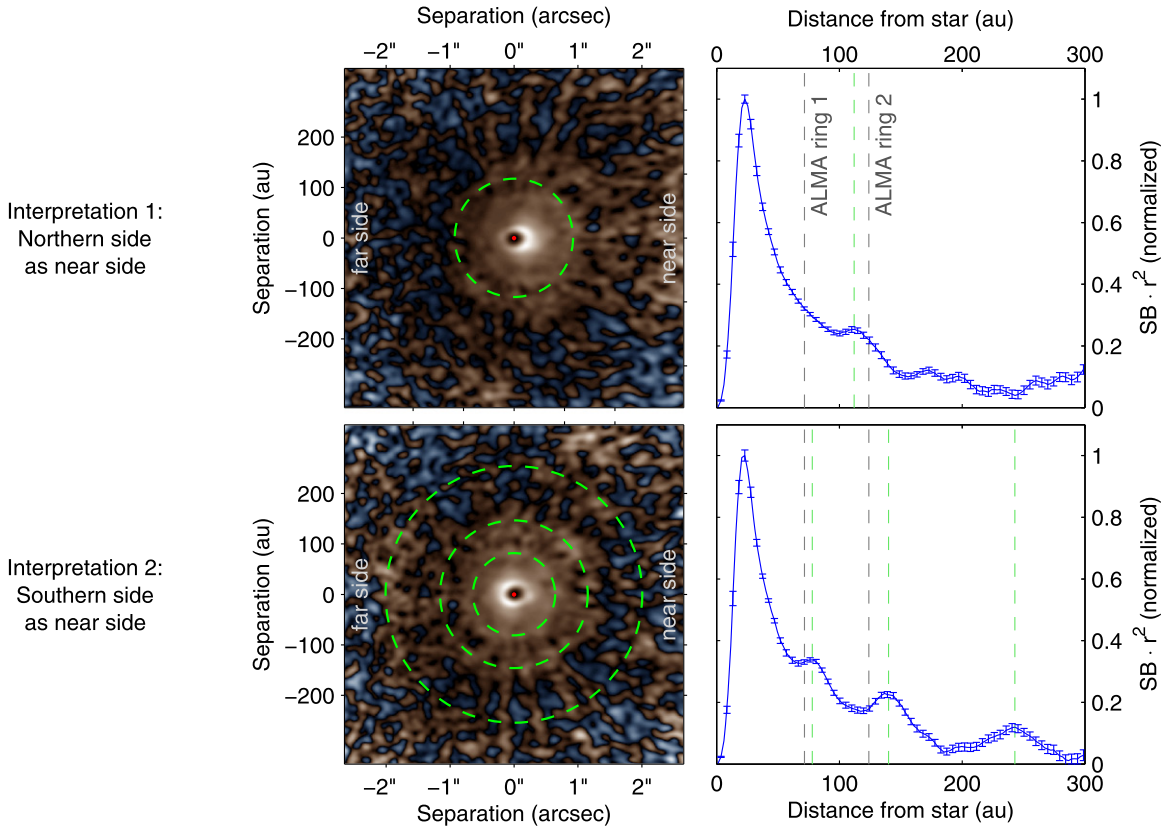

Figure 8. Two possible deprojections of AS 209 using $i = 35.^{\circ}3$ and P.A. $= 86.^{\circ}0$, as determined by Fedele et al. (2017), as well as $h/r(100\,\mathrm{au}) = 0.1617$ and $\alpha = 1.219$ (the average values determined for these parameters in Section 4.3). The first (upper) deprojection assumes the northern side to be the near side, while the second assumes the southern side to be the near side (i.e., P.A. $= 86.^{\circ}0 + 180.^{\circ}0$ in our frame of reference). The frames on the left show the deprojected images displayed in linear stretch after scaling with r^2, while the plots on the right show azimuthally averaged surface brightness, also scaled with r^2 and normalized to the peak. Rings are detected at around either 112 au (interpretation 1) or 78, 140, and 243 au (interpretation 2) and marked with green dashed lines. The ALMA continuum rings seen by Fedele et al. (2017) at 72 and 124 au are marked with gray dashed lines. The 1σ error bars are calculated from the U_ϕ frames, taking into account that the effective beam size changes when deprojecting (see the Appendix for a detailed description of our error derivations). They do not take into account azimuthal variations in the Q_ϕ frame. The dashed lines in the left panel show the position of rings detected in scattered light.

et al. 2003) because the AO correction was not good enough to produce a visible Airy ring pattern.

Andrews et al. (2009) found an inclination of ≈38° along a P.A. of ≈86°. A more accurate measurement of inclination and position angle (≈35.°3 and ≈86.°0, respectively) has been provided recently by Fedele et al. (2017). The latter authors also detected rings in the ALMA submillimeter continuum at 72 and 124 au, along with gaps at 59 and 98 au, but neither can determine which is the near side of the disk.

Motivated by this, we deproject our disk using the aforementioned parameters (Fedele et al. 2017), as well as the average flaring of our disks determined in Section 4.3 (h/r (100 au) = 0.1617 and $\alpha = 1.219$). We present both possible interpretations, with either the northern or southern side being the near side, in Figure 8. Given the low overall S/N of our data, we use the H band and a smoothing kernel of 125 mas. In both cases, we detect surface brightness enhancements, either at 112 au (northern side as near side) or at 78, 140, and 243 au (southern side as near side). The first interpretation is consistent with the fact that for all of our other disks, the near side is the brighter side (see Figure 4) as well as the location of the bright spots near the coronagraph on the northern side. The detected scattered-light ring is also just inside the ring in the submillimeter detected with ALMA, as is typical (e.g., Garufi et al. 2014; Bertrang et al. 2018).

However, inspecting the image before deprojection (see Figure 2), faint rings are visible in the H-band image that are displaced toward the northern side, which argues for interpretation 2, with the southern side being the near side. This is supported by the fact that we detect more rings at higher contrasts. In fact, specifically, the inner faint ring visible by eye can still be seen in the first deprojection (interpretation 1, Figure 8), distorted toward the right side. We also know cases where the far side is the brighter side in polarimetric scattered light, for example, HD 100546 (Avenhaus et al. 2014a; Garufi et al. 2016) and PDS 70 (Hashimoto et al. 2012; Keppler et al. 2018). At this point, we cannot determine which interpretation is correct, given that there are valid arguments for either, but in both interpretations, the disk displays ring structures. The detection of the rings is relatively robust with regard to the flaring angle: the same rings are detected with constant flaring angles between $h/r = 0.1$ and 0.3, with no significant changes in their locations. Assuming no flaring ($h/r = 0$, flat disk) or without performing any deprojection, no rings are detected (see also Figure 3).

The size of the disk in the millimeter continuum varies with wavelength, with the disk being larger at shorter wavelengths (∼1″/121 au at 0.88 mm; Pérez et al. 2012). At about this radius, there is a ringlike enhancement in CO emission described by Huang et al. (2016), i.e., at a radius similar to that of the outer ring reported in Fedele et al. (2017). These

authors propose CO desorption near the edge of the millimeter disk as a possible explanation of this enhancement. While the S/N of our observations decreases rapidly beyond the inner parts of the disk, we trace faint vestiges of scattered light out to ≈200 au and possibly extending beyond (see Figure 3), meaning that while the disk is unremarkable and relatively faint in scattered light, it is not actually very small compared to the other disks. This is consistent with the fact that CO gas emissions can be traced beyond the diameter of the millimeter disk and further supports the notion of the maximum dust grain size decreasing with radius, as μm-sized grains can be detected at these large radii, while millimeter-sized grains cannot (Pérez et al. 2012; Tazzari et al. 2016).

5.3. Possible Companions

While our setup was not optimized for the detection of point sources, we reach a deep background limit (≈25 mag in the *H* band and ≈25.5 mag in the *J* band at 2″ separation, on average) thanks to the good performance of the SPHERE/IRDIS AO/coronagraph system and long integration times combined with the fact that our primary targets are relatively faint. Consequently, additional point sources can be seen in the total intensity images of all of our data sets, ranging from one or two up to >40 for the V4046 Sgr data set. Background sources are to be expected at these magnitudes, specifically in cases like V4046 Sgr, which lies close to the galactic plane. Thus, we expect most, if not all, of these point sources to be background objects.

However, two objects seemed particularly interesting: a point source toward the northeast, just outside the disk rim of IM Lup, and an object toward the west at a separation of ∼1.″1 of RU Lup (see Figure 9). The point source close to IM Lup can clearly be shown to be not comoving using archival NACO data (it does not appear in the archival *HST* data used to first detect the disk from Pinte et al. 2008, presumably because the point source was behind the disk at that epoch). In fact, this point source was already previously analyzed and shown to be a background source by Mawet et al. (2012). For RU Lup, no such archival data were available, but a short exposure 1 yr later showed that the object is most likely a background object.

We did not perform follow-up observations or literature checks for the remaining point sources. However, our data can serve as additional reference points for future studies trying to detect companions to these stars.

5.4. Correlation of Disk and Stellar Parameters

Our sample was set up to span a large range in stellar ages, in order to be able to investigate possible evolutionary steps in protoplanetary disks. Our sample also covers a certain range in stellar masses/spectral types, and comparison to existing studies of Herbig Ae/Be stars (Muto et al. 2012; Wagner et al. 2015; Ginski et al. 2016; Monnier et al. 2017; Bertrang et al. 2018, and many others) broadens this range considerably.

However, even though all eight disks we observed could be detected, most of them over a large range of radii, in two different wavelengths, and even though they show a large diversity in structure and physical size, no clear trends with either age or spectral type can be determined. This argues for a scenario in which the formation and evolution of protoplanetary disks and their interplay with planet formation is a complex and chaotic process in which other factors, such as the formation environment, may also play important roles, in agreement with theoretical studies of disk evolution (Bate 2018). Rather than being examples of a more or less well-defined sequence of evolutionary steps, we might be looking at different evolutionary pathways; for example, some of the disks we investigate may be forming (or have already formed) gas giant planets, while others are only forming smaller, rocky worlds (Williams & Cieza 2011; Cieza et al. 2015; Owen 2016), even though we do not detect correlations with the submillimeter flux either. This scenario is well in line with the fact that the outcome of planet formation is very diverse, as evidenced by the *Kepler* results (Borucki et al. 2010; Batalha et al. 2013; Mullally et al. 2015). However, we have to keep in mind that the sample was not chosen as an unbiased sample but was based on high (sub)millimeter excesses, so it is possible that the older disks represent atypical examples, and that there exist underlying correlations we have yet to discover.

Comparing our data to existing studies of both T Tauri and Herbig stars, there is one peculiarity, though: while spiral features are relatively abundant in Herbig systems (Hashimoto et al. 2011; Avenhaus et al. 2014a, 2017; Benisty et al. 2015; Ohta et al. 2016; Stolker et al. 2016; Long et al. 2017), none of our systems show clear signs of spiral structures. Instead, five out of eight of our systems are clearly dominated by ring structures, with a sixth (AS 209) showing low-S/N ring structures as well. On top of that, DoAr 44 shows a bright inner ring and possibly weaker ringlike structures further out. The only system to not show any ring structures (or any structures whatsoever) is RU Lup, but this could potentially be due to the fact that the low S/N achieved for this disk does not allow for the detection of any substructures.

6. Conclusion

In this work, we show the first results of our DARTTS survey and present eight T Tauri disks imaged with SPHERE/IRDIS in PDI mode at high S/N. All eight disks are clearly detected. The disks show remarkable differences in their total extent and the amount of substructures they show, with two disks (RU Lup and AS 209) appearing particularly faint compared to the others. However, there are no significant differences in the two filters for each source.

We are able to see the three-dimensional structure of three of our disks (IM Lup, RXJ 1615, and MY Lup) because we detect the lower disk surface and are able to infer the three-dimensional structure, i.e., the flaring of the $\tau = 1$ surface layer, for two more (V4046 Sgr and PDS 66) by means of fitting inclined and elevated rings to their scattered-light images. This way, we can also show that the rings seen in these images are highly consistent with circles (rather than ellipses) that are inclined and displaced horizontally off the disk midplane. We can also show that most T Tauri disks seem to follow approximately the same flaring law for their $\tau = 1$ surfaces. The flaring indices we derive range from $\alpha = 1.116 \pm 0.095$ to $\alpha = 1.605 \pm 0.132$, but it is possible to approximately fit the data for all of our sources together with a flaring index of $\alpha = 1.219 \pm 0.026$ and $h/r(100\,\mathrm{au}) = 0.1617 \pm 0.0051$.

This work once again shows the remarkable power of PDI, specifically when combined with the power of a high-performance AO system such as SPHERE. High S/N can be achieved thanks to high Strehl ratios in the *H* band even for stars as faint as $R = 12$ (in medium-to-good conditions). In this

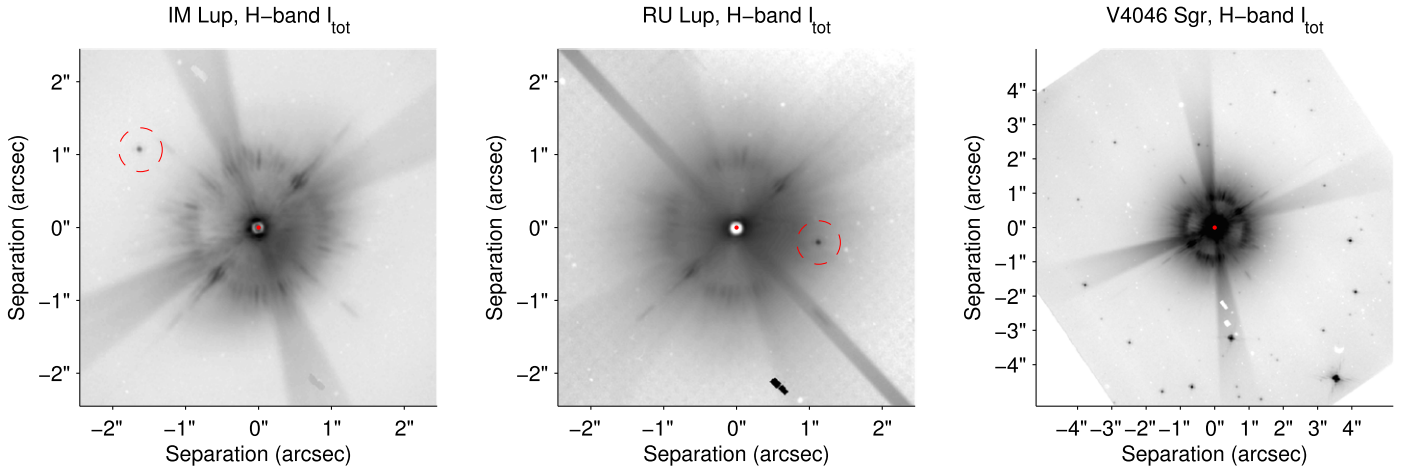

Figure 9. Point-source detections in the total intensity images (no PSF subtraction) of our sources. Left and middle: Point sources close to the disks of IM Lup and RU Lup (circled in red). Both of these point sources were confirmed to not be comoving using literature or follow-up data. The IM Lup point-source was already confirmed to be a background source by Mawet et al. (2012). Right: V4046 Sgr showing >40 point sources in its vicinity, most or all of which are expected to be background sources, given the position of V4046 Sgr on the sky very close to the galactic plane. The scaling is chosen in all cases to make the point sources most clearly visible. North is up and east is to the left in all three frames.

stellar demographic, SPHERE has an advantage compared to instruments such as the GPI, which is limited to stars of $I \lesssim 9$. All of our targets are fainter than magnitude 9 in the I band. V4046 Sgr is close ($I = 9.11$) and has been imaged with the GPI (Rapson et al. 2015a), but our images have significantly higher S/N.

While a full in-depth discussion of all of our targets is beyond the scope of this paper, such analyses are already underway and will be published separately (e.g., Casassus et al. 2018; V. d'Orazi et al. 2018, in preparation). Other targets have already been discussed in detail in the literature (e.g., de Boer et al. 2016).

For a full understanding of our targets, submillimeter observations—specifically high-resolution ALMA data—will be crucial. Efforts to obtain such data are underway under the ALMA subpart of our survey (DARTTS-A, led by Sebastian Perez). Combined with such observations, the results for the eight T Tauri stars presented in this paper, along with further DARTTS T Tauri star observations to be presented in a future paper, will lead to a significant step forward in our understanding of T Tauri disks.

SPHERE is an instrument designed and built by a consortium consisting of IPAG (Grenoble, France), MPIA (Heidelberg, Germany), LAM (Marseille, France), LESIA (Paris, France), Laboratoire Lagrange (Nice, France), INAF–Osservatorio di Padova (Italy), Observatoire de Gen'eve (Switzerland), ETH Zurich (Switzerland), NOVA (Netherlands), ONERA (France), and ASTRON (Netherlands), in collaboration with ESO. SPHERE also received funding from the European Commission Sixth and Seventh Framework Programmes as part of the Optical Infrared Coordination Network for Astronomy (OPTICON) under grant number RII3-Ct-2004-001566 for FP6 (20042008), grant number 226604 for FP7 (20092012), and grant number 312430 for FP7 (20132016).

HA acknowledges support from the Millennium Science Initiative (Chilean Ministry of Economy) through grant RC130007 and further financial support by FONDECYT, grant 3150643. Part of this work has been carried out within the framework of the National Centre for Competence in Research PlanetS, supported by the Swiss National Science Foundation. HA, SPQ, and HMS acknowledge the financial support of the SNSF. GH-MB acknowledges financial support from CONICYT through FONDECYT grant 3170657. CC acknowledges support from project CONICYT PAI/Concurso Nacional Insercion en la Academia, convocatoria 2015, folio 79150049, and financial support from ICM Nucleo Milenio de Formacion Planetaria, NPF. MB acknowledges funding from ANR of France under contract number ANR-16-CE31-0013 (Planet Forming Disks). CP acknowledges funding from the Australian Research Council (ARC) under Future Fellowship number FT170100040. SC and SP acknowledge financial support from CONICYT FONDECYT grant 1171624. Financial support was provided by Millennium Nucleus RC130007 (Chilean Ministry of Economy). SP acknowledges CONICYT-Gemini grant 32130007.

This research has made use of the SIMBAD database, operated at CDS, Strasbourg, France. This work has furthermore made use of data from the European Space Agency (ESA) mission *Gaia* (http://www.cosmos.esa.int/gaia), processed by the *Gaia* Data Processing and Analysis Consortium (DPAC; http://www.cosmos.esa.int/web/gaia/dpac/consortium). Funding for the DPAC has been provided by national institutions, in particular the institutions participating in the *Gaia* Multilateral Agreement.

We thank the staff at the VLT for their excellent support during the observations. We also would like to thank our anonymous referee for comments that helped to improve this paper.

Facility: VLT:Melipal (SPHERE).

Appendix
Data Reduction Pipeline

This appendix describes the data reduction pipeline used for the reduction of all data used in this paper and potentially future papers making use of either SPHERE/IRDIS or SPHERE/ZIMPOL. It is an updated and improved version of the NACO data reduction pipeline described in Avenhaus et al.

(2014b), but we think that the number of changes to the pipeline implemented since then warrants describing the entire pipeline in detail again. The goal of the pipeline is to provide the most self-consistent, best-S/N data reduction of the input data possible, and our goal was to be able to reduce all data using (mostly) the same parameters, in order to make the results less parameter-dependent.

A.1. Data Preparation and Cosmetics

There are a total of five types of input frames used for our pipeline: dark frames, flat frames, flux frames, center frames, and science frames.

As a preparation step, the dark frames and flat frames are converted to master dark frames and master flat frames using the official ESO SPHERE esorex pipeline recipes. This process also produces bad-pixel maps (BPMs), which are later used to identify bad detector pixels. The master files are then applied to the flux, center, and science frames in the same fashion. Bad pixels are corrected by filling them with Gaussian-smoothed values from surrounding good pixels. On top of the pixels identified in the BPMs, outliers with regard to the local flux (`>badPixelSigmaCut`; we use 10σ here) are also treated as bad pixels in this process. Bad pixels that are more than 2 pixels away from any good pixel are not corrected and are instead set to *NaN*.

The results are preprocessed and cleaned flux, center, and science frames. These three frames have the following purposes.

1. Flux frames: These frames are taken with the star displaced from the coronagraph. The purpose is to provide both an estimate of the PSF during the observation and a measurement of the flux of the star.
2. Center frames: These frames are taken behind the coronagraph but with a pattern overlaid on the deformable mirror (DM) that produces four bright spikes well outside the coronagraph. These spikes can be used to accurately determine the position of the star behind the coronagraph.
3. Science frames: These frames contain the actual science data.

A.2. Determining the Position of the Star

The position of the star in both the ordinary and extraordinary beams is determined using the center frames mentioned before. In a first step, the *center guess* is roughly determined by smoothing the image with a very large Gaussian kernel and finding the peak. In a second step, the data between a radius of `centering_inner_crop` and `centering_outer_crop` around this *center guess* are extracted (the rest of the data are set to *NaN*), and the median is subtracted to get the background to approximately zero. The image is then radon-transformed, and the peak of this radon transform is converted back into the location of the star in the image plane. The process is then repeated with the newly determined center used as the *center guess* for a second iteration.

As we take a center frame both before and after the observations, we average the position of the star between these two. The difference between the stellar position before and after the science frames are taken is usually small, on average 0.23 pixels (2.8 mas) for the *H*-band data and 0.20 pixels (2.5 mas) for the *J*-band data.

A.3. Reduction of Science Frames

In a first step, the prereduced science frames are upscaled by a factor of `scaling` using bicubic interpolation. This is done in order to reduce uncontrollable smoothing effects from shifting the images by fractions of pixels further in the data reduction. In this step, the slight difference in pixel scale between the two detector directions (`IRDIS_anamorphism`) is also corrected. The data are then centered to the (appropriately scaled) predetermined position of the star and fine-centered using cross-correlation between the ordinary and extraordinary beams (this works well because the data are dominated by the unpolarized stellar halo, and the coronagraph produces a sharp edge). After this, the images are aligned to true north using the known true north of the instrument (`IRDIS_trueNorth`) and the instrument position angle the data were taken with. At this point, the data are corrected for dark and flat frames, accurately centered, north-aligned, and prescaled. In the case of our data for this paper, we checked whether the scaling parameter had any significant effect and found out that it does not. We thus keep the scaling at 1 for reasons of performance.

A.3.1. Precorrection for Instrumental Polarization

There are two popular methods that have been used to correct for instrumental polarization in PDI data: equalizing the flux in the ordinary and extraordinary beams before calculating the Stokes vectors (e.g., Avenhaus et al. 2014b) and subtracting a polarized halo of the star in order to minimize U_ϕ after the calculation of the Stokes vectors, as pioneered by the SEEDS team (e.g., Follette et al. 2015). Both of these methods assume the star to be intrinsically unpolarized. This is not necessarily justified: stellar spots can produce intrinsic polarization, and polarized absorption from the disk or a halo can produce polarization. On top of that, there could be interstellar polarization. However, we currently do not know how to (a) accurately determine the polarization of the star and (b) deal with it if we did. It is worth mentioning several things, though. First, the polarization of stars is usually low ($\ll$10%) compared to the scattering polarization (15%–50%) of the disk, so it is likely a second-order effect. Second, interstellar polarization is expected to be low due to the proximity of these stars and, furthermore, affects both the star and the disk, and as such it affects our data in exactly the same way as global instrumental polarization. It would thus just be canceled out by our correction routines.

That being said, we in fact use both the pre-Stokes correction and post-Stokes correction methods in our pipeline. The reason is that the post-Stokes correction method can be better fine-tuned and is in general more accurate, but it fails in the case of data taken under adverse observing conditions and faint disks (in our case, specifically RU Lup). We thus use the pre-Stokes correction method (described here) as a means of precorrection and the post-Stokes correction method (see below) as a means of fine-correcting, combining the strengths of both techniques.

For the precorrection, the flux in the ordinary and extraordinary beams is measured in an annulus between `correctInst_preCorrect_Rinner` and `correctInst_preCorrect_Router`, and the ratio between the two fluxes is

Table 7
Reduction Parameters

Parameter	Value
badPixelSigmaCut	10σ
centering_inner_crop	400 mas (J band)/500 mas (H band)
centering_outer_crop	500 mas (J band)/670 mas (H band)
scaling	1
IRDIS_anamorphism	[1.006 1]
IRDIS_trueNorth	$-1\overset{\circ}{.}775$ (east of north)
correctInst_preCorrect_Rinner	0 mas
correctInst_preCorrect_Router	1000 mas
IRDIS_pixelscale	12.258 mas pixel^{-1}

Note. Parameters used in data reduction for this paper. The negative angle for true north means that in order to correct for true north, the images have to be rotated clockwise by $1\overset{\circ}{.}775$.

determined. The flux is then equalized by multiplying one of the beams by sqrt(ratio) and the other by sqrt(1/ratio).

A.3.2. Stokes Calculation and Stacking

The Stokes vectors Q and U are calculated in the standard way (Tinbergen 2005). The formulas used are

$$p_{\rm q} = \frac{R_Q - 1}{R_Q + 1}, \qquad p_{\rm u} = \frac{R_U - 1}{R_U + 1},$$

with

$$R_Q = \sqrt{\frac{I^{0^\circ}_{\rm ord}/I^{0^\circ}_{\rm extra}}{I^{-45^\circ}_{\rm ord}/I^{-45^\circ}_{\rm extra}}}, \qquad R_U = \sqrt{\frac{I^{-22\overset{\circ}{.}5}_{\rm ord}/I^{-22\overset{\circ}{.}5}_{\rm extra}}{I^{-67\overset{\circ}{.}5}_{\rm ord}/I^{-67\overset{\circ}{.}5}_{\rm extra}}}.$$

Here the subscripts refer to either the ordinary or extraordinary beams, and the superscripts refer to the angular position of the HWP. The Stokes Q and U parameters are then simply calculated as

$$Q = p_{\rm q} \ * \ I_Q, \qquad U = p_{\rm u} \ * \ I_U,$$

where

$$I_Q = (I^{0^\circ}_{\rm ord} + I^{0^\circ}_{\rm extra} + I^{-45^\circ}_{\rm ord} + I^{-45^\circ}_{\rm extra})/2,$$
$$I_U = (I^{-22\overset{\circ}{.}5}_{\rm ord} + I^{-22\overset{\circ}{.}5}_{\rm extra} + I^{-67\overset{\circ}{.}5}_{\rm ord} + I^{-67\overset{\circ}{.}5}_{\rm extra})/2.$$

are the total intensities in the images used for the calculation of $p_{\rm q}$ and p_U. The Stokes vectors for each individual HWP cycle (typically between 4 and 10) are then stacked together using the mean of the individual frames.

A.3.3. Fine Correction for Instrumental Polarization and Local Stokes Vectors

The second (post-Stokes) correction for instrumental polarization is integrated with the calculation of the local Stokes vectors Q_ϕ and U_ϕ, defined as

$$Q_\phi = +Q\cos 2\theta + U\sin 2\theta,$$
$$U_\phi = -Q\sin 2\theta + U\cos 2\theta,$$
$$\theta = \arctan\frac{x - x_0}{y - y_0} + \gamma.$$

The reason these two steps are integrated with each other is that in order to perform the fine correction for instrumental polarization, U_ϕ needs to be calculated multiple times in an iterative process. Furthermore, during the optimization described below, γ, which is the correction for a possible misalignment of the HWP or otherwise rotated polarization, can also be determined.

The SEEDS team (Follette et al. 2015) uses a scaled version of the intensity image ($I = I_Q + I_U$), which is added to the Stokes vectors Q and U, in order to minimize the absolute signal in U_ϕ. We expand on this idea and add constants on top of this, such that the calculation of Q_ϕ and U_ϕ becomes

$$Q_\phi = +Q^\star\cos 2\theta + U^\star\sin 2\theta;$$
$$U_\phi = -Q^\star\sin 2\theta + U^\star\cos 2\theta;$$
$$\theta = \arctan\frac{x - x_0}{y - y_0} + \gamma,$$

with

$$Q^\star = Q + c1\cdot I + c2, \qquad U^\star = U + c3\cdot I + c4.$$

This gives a total of five variables ($c1$, $c2$, $c3$, $c4$, and γ) that are optimized in order to minimize the absolute signal in U_ϕ, i.e., $\sum|U_\phi|$, between an inner and outer radius, postStokesCorr_rInner and postStokesCorr_rOuter (listed in Table 8). The radii used depend on the geometry of the source but are kept the same between the two bands for consistency. For the optimization, the MATLAB built-in routine fminsearch is used.

The reason we use a constant on top of the scaled intensity image is that we know that the polarization of the target (due to interstellar or intrinsic polarization) is not necessarily equal to the polarization of the sky background. The constant allows for separate correction of the sky background, and our experiments show that this makes a significant difference, particularly for suppressing a butterfly pattern otherwise appearing in both Q_ϕ and U_ϕ at large separations.

Note that this procedure can, in principle, remove (astrophysical) signals in the form of butterfly patterns from the U_ϕ image. However, the butterfly patterns that can be created by adding constants and multiples of the total intensity frame to

Table 8
Instrumental Polarization Correction Radii

Target	postStokesCorr_rInner	postStokesCorr_rOuter
IM Lup	0.5	3.5
RXJ 1615	0.0	3.5
RU Lup	0.0	3.5
MY Lup	1.0	3.5
PDS 66	0.5	3.5
V4046 Sgr	0.0	3.5
DoAr 44	0.5	3.5
AS 209	0.5	3.5

Note. Inner and outer correction radii for the second part of the instrumental polarization correction (in arcseconds).

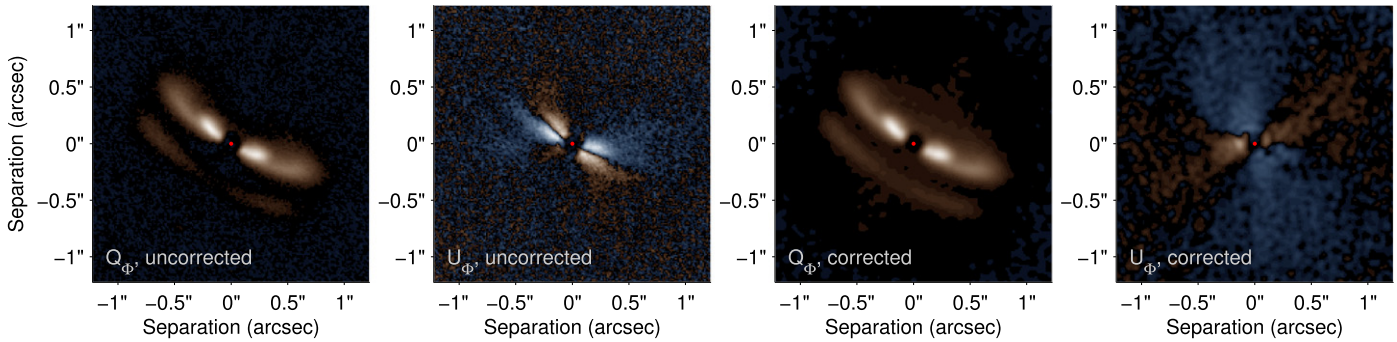

Figure 10. Example of the effects of self-cancellation and Q_ϕ/U_ϕ cross-talk correction (from left to right: Q_ϕ, U_ϕ, $Q_{\phi,\mathrm{corrected}}$, $U_{\phi,\mathrm{corrected}}$). While the correction on Q_ϕ mostly has the effect of making the disk brighter, especially in the inner regions, the correction on U_ϕ removes the strong butterfly-like pattern, which could be misinterpreted as a residual signal from multiple scattering, similar to what is expected theoretically (Canovas et al. 2015), though with the opposite sign, which could potentially help to distinguish these effects. The U_ϕ images have been scaled up by a factor of 5 to make the fainter signal with regard to Q_ϕ visible. Blue hues correspond to negative values, brown hues to positive values. While the total flux in U_ϕ remains largely unchanged, with the mean being around zero, the standard deviation is significantly reduced, by a factor of 2.14. North is up and east is to the left.

the Q and U frames are very limited and unlikely to match astrophysical signals well. Indeed, the butterfly-like signal in the MY Lup U_ϕ frame (see Figure 10), though not astrophysical in nature (see next paragraph), is not removed.

To convert the images to a physical scale, we use the `IRDIS_pixelscale` of 12.258 mas pixel^{-1} and the distances to our targets acquired from the literature.

A.4. Correction for PDI Self-cancellation and Q_ϕ/U_ϕ Cross-talk

At this point, the corrected data are still affected by two effects that we know of, which are inherent to PDI and can lead to misinterpretation of the data: PDI self-cancellation and Q_ϕ/U_ϕ cross-talk.

PDI self-cancellation has been discussed before and stems from the fact that, close to the position of the star, the positive and negative signals from the butterfly patterns in both the Stokes Q and U vectors cancel each other out due to being smeared out by the PSF of the telescope. A description of this effect, together with an example, can be found in Avenhaus et al. (2014a).

The Q_ϕ/U_ϕ cross-talk has not, to our knowledge, been discussed before. The decomposition into Q_ϕ and U_ϕ relies on knowledge of the position angle in the field, but the flux from one point in the sky is distributed over an area due to the PSF. This leads to the usage of an incorrect position angle for the decomposition, which in turn leads to incorrect results. Unfortunately, the patterns produced by this effect can, especially for highly inclined disks, resemble the patterns theoretically expected from multiple scattering effects in such disks, which makes them prone to misunderstanding. The effect clearly shows up in our data on V4046 Sgr, as seen in Figure 10.

While an exhaustive discussion of possible corrections for these effects will be presented in a separate paper (H. Avenhaus et al. 2018, in preparation), we want to briefly describe how we deal with the effect here. Both effects stem from the fact that the resolution in our images is finite and limited by the telescope PSF. If we could image Q and U at infinite resolution, neither of the effects would occur.

Thus, we use the following method to correct our data. First, we deconvolve the corrected Q and U data using Wiener deconvolution, using the PSF obtained from the flux frames. These data then have very high resolution and very low S/N, because deconvolution strongly increases the noise. From these Q and U frames, we calculate Q_ϕ and U_ϕ, which are both also unusably noisy. We then reconvolve these images, which brings the resolution back to the level we had before while also bringing the noise back to a similar level. Assuming we use the right PSF, this process brings us very close to the actual signal (in theory, in the absence of noise and without a coronagraph, the reconstruction is perfect). Another benefit is that we do not have to use the same PSF to reconvolve but can choose another PSF (for example, one with finite support or a Gaussian of known FWHM). In addition to the original PSF, we use Gaussians with FWHMs of 50, 75, 100, and 125 mas for this purpose, allowing us to compare the disks at similar resolution.

As far as we can tell (also by applying this technique to simulated data), this method works remarkably well but depends on the quality of the PSF. As can be seen in Figure 10, this affects both the Q_ϕ and U_ϕ signals. While the Q_ϕ signal is mostly getting suppressed by the self-cancellation effect, with the Q_ϕ/U_ϕ cross-talk having no perceptible impact, the U_ϕ clearly is affected by Q_ϕ/U_ϕ cross-talk (prone to possible misinterpretation in terms of multiple scattering). It is thus of vital importance to understand this effect and correct for it.

A.5. Error Estimation

Since both the Q_ϕ and U_ϕ frames are affected by noise (readout noise, speckle noise, systematics) in a similar way, but U_ϕ is largely devoid of signal, we use the variance in the U_ϕ frame in order to estimate the noise. If there is any astrophysical signal in the U_ϕ frame, this method will be conservative, because it overestimates rather than underestimates the noise in this case.

Throughout this paper, we estimate errors for image areas (such as annuli around the star), rather than for point sources. This means that we can take advantage of the fact that errors will tend to average out over larger image areas. Our standard deviation for the mean flux in an image area A thus becomes

$$\sigma_\mathrm{A} = \sqrt{\frac{\mathrm{var}(U_{\phi,\mathrm{A}})}{N}},$$

where $\mathrm{var}(U_{\phi,\mathrm{A}})$ is the variance in the U_ϕ frame over the respective area, and N is the number of resolution elements in

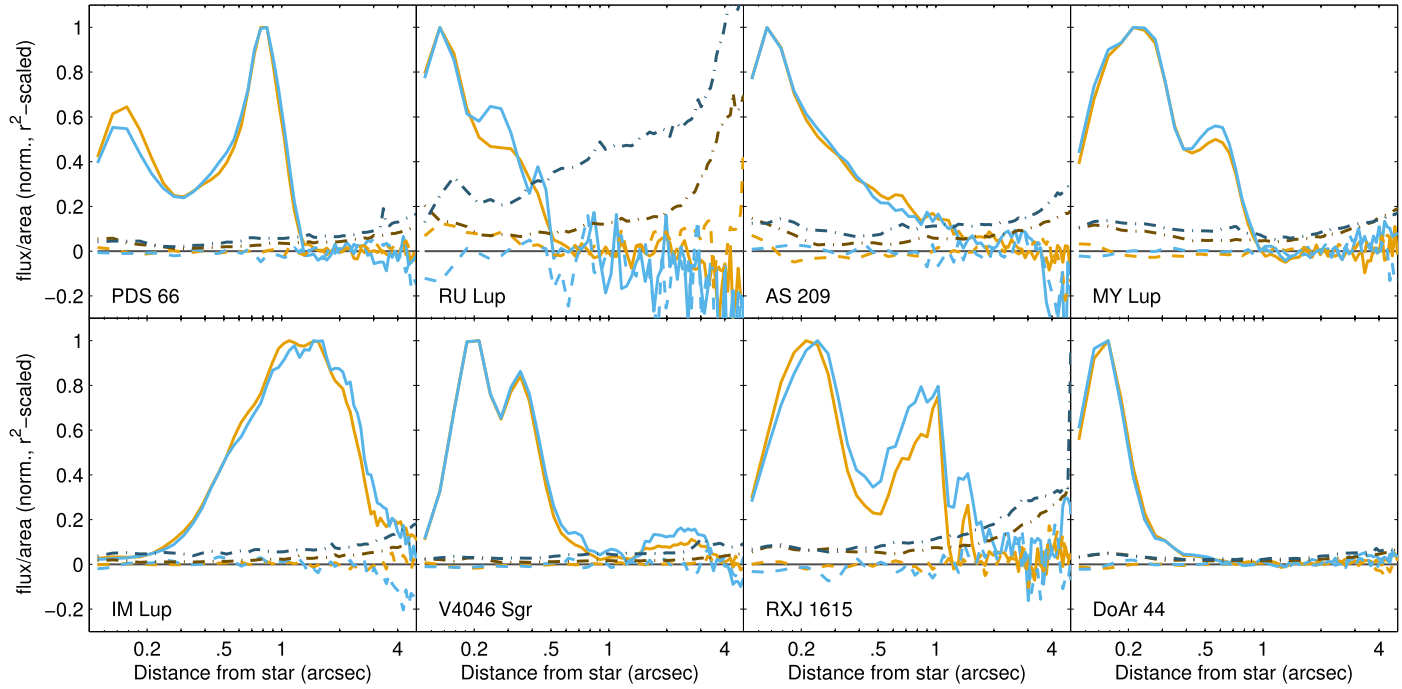

Figure 11. Individual normalized Q_ϕ and U_ϕ surface brightness plots vs. distance for all of our targets. Orange lines present H-band and blue lines J-band data. Solid lines represent Q_ϕ, and dashed lines represent U_ϕ. Darker dash-dotted lines represent 3σ detection limits. The width of the annuli used for averaging increases with radius proportional to $r^{1/2}$ (similar to Figure 3). Note the logarithmic stretch of the x-axis. The data have been scaled with r^2 in order to improve readability.

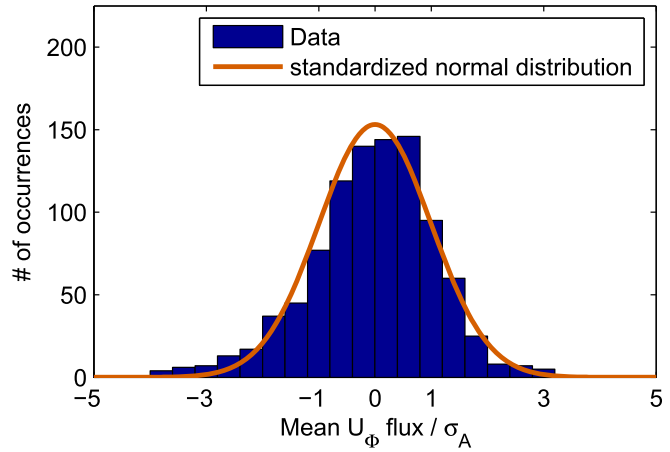

Figure 12. Mean U_ϕ flux across all annuli used to calculate the surface brightnesses in Figure 11, divided by the respective error estimate σ_A. The data follow a standardized normal distribution reasonably well, with some additional outliers.

the area. This method ensures that our error estimates are independent of the kernel we use for reconvolution (see above), as wider kernels will lead to stronger smoothing but also to fewer resolution elements.

Given that we correct U_ϕ to be zero, on average, we can then expect the distribution of mean fluxes in U_ϕ across many areas, divided by their respective σ_A, to approximately follow a standardized normal distribution. We use this as a sanity check. We show that this is approximately correct in Figures 11 and 12. The mean signal of U_ϕ across a total of 960 areas (annuli) surpasses 3σ only three times. The distribution does follow the standardized normal distribution reasonably well, with only a few additional outliers, even though we do not correct U_ϕ over the entire separation range (0.″1–5.″2) but rather only between the inner and outer radii specified in Table 8. However, the Shapiro–Wilk test clearly shows that this is not a Gaussian distribution (p-value $\approx 1.5 \cdot 10^{-9}$). The outliers are mostly from the very inner and outer regions: restricting our analysis to separations between 0.″5 and 3.″5, the distribution of $\overline{U_{\phi,A}}/\sigma_A$ is indistinguishable from a Gaussian distribution (576 annuli, p-value ≈ 0.2).

ORCID iDs

Sascha P. Quanz https://orcid.org/0000-0003-3829-7412
Sebastian Perez https://orcid.org/0000-0003-2953-755X
Simon Casassus https://orcid.org/0000-0002-0433-9840
Christophe Pinte https://orcid.org/0000-0001-5907-5179
Gesa H.-M. Bertrang https://orcid.org/0000-0001-5127-0172
Claudio Caceres https://orcid.org/0000-0002-6617-3823
Myriam Benisty https://orcid.org/0000-0002-7695-7605
Carsten Dominik https://orcid.org/0000-0002-3393-2459

References

Ababakr, K. M., Oudmaijer, R. D., & Vink, J. S. 2017, MNRAS, 472, 854
Akiyama, E., Hashimoto, J., Liu, H. B., et al. 2016, AJ, 152, 222
Alcalá, J. M., Manara, C. F., Natta, A., et al. 2017, A&A, 600, A20
ALMA Partnership, Brogan, C. L., Pérez, L. M., et al. 2015, ApJL, 808, L3
Andre, P., & Montmerle, T. 1994, ApJ, 420, 837
Andrews, S. M., Rosenfeld, K. A., Kraus, A. L., & Wilner, D. J. 2013, ApJ, 771, 129
Andrews, S. M., & Williams, J. P. 2005, ApJ, 631, 1134
Andrews, S. M., Wilner, D. J., Espaillat, C., et al. 2011, ApJ, 732, 42
Andrews, S. M., Wilner, D. J., Hughes, A. M., Qi, C., & Dullemond, C. P. 2009, ApJ, 700, 1502
Andrews, S. M., Wilner, D. J., Zhu, Z., et al. 2016, ApJL, 820, L40
Ansdell, M., Williams, J. P., van der Marel, N., et al. 2016, ApJ, 828, 46
Anthonioz, F., Ménard, F., Pinte, C., et al. 2015, A&A, 574, A41
Avenhaus, H., Quanz, S. P., Meyer, M. R., et al. 2014a, ApJ, 790, 56
Avenhaus, H., Quanz, S. P., Schmid, H. M., et al. 2014b, ApJ, 781, 87
Avenhaus, H., Quanz, S. P., Schmid, H. M., et al. 2017, AJ, 154, 33

Batalha, N. M., Rowe, J. F., Bryson, S. T., et al. 2013, ApJS, 204, 24
Bate, M. R. 2018, arXiv:1801.07721
Beckwith, S. V. W., Sargent, A. I., Chini, R. S., & Guesten, R. 1990, AJ, 99, 924
Benisty, M., Juhasz, A., Boccaletti, A., et al. 2015, A&A, 578, L6
Bertrang, G. H.-M., Avenhaus, H., Casassus, S., et al. 2018, MNRAS, 474, 5105
Beuzit, J.-L., Feldt, M., Dohlen, K., et al. 2008, Proc. SPIE, 7014, 701418
Borucki, W. J., Koch, D., Basri, G., et al. 2010, Sci, 327, 977
Canovas, H., Ménard, F., de Boer, J., et al. 2015, A&A, 582, L7
Carpenter, J. M., Ricci, L., & Isella, A. 2014, ApJ, 787, 42
Carpenter, J. M., Wolf, S., Schreyer, K., Launhardt, R., & Henning, T. 2005, AJ, 129, 1049
Casassus, S., Avenhaus, H., Pérez, S., et al. 2018, MNRAS, 477, 5104
Casassus, S., Perez, M. S., Jordán, A., et al. 2012, ApJL, 754, L31
Chiang, E. I., & Goldreich, P. 1997, ApJ, 490, 368
Cieza, L., Williams, J., Kourkchi, E., et al. 2015, MNRAS, 454, 1909
Cleeves, L. I., Öberg, K. I., Wilner, D. J., et al. 2016, ApJ, 832, 110
Cohen, M., & Kuhi, L. V. 1979, ApJS, 41, 743
Comerón, F. 2008, in Handbook of Star Forming Regions, Vol. II: The Southern Sky, ed. B. Reipurth (San Francisco, CA: ASP) 295
Cortes, S. R., Meyer, M. R., Carpenter, J. M., et al. 2009, in AIP Conf. Ser. 1158, Exoplanets and Disks: Their Formation and Diversity, ed. T. Usuda, M. Tamura, & M. Ishii (Melville, NY: AIP), 119
de Boer, J., Salter, G., Benisty, M., et al. 2016, A&A, 595, A114
de Zeeuw, P. T., Hoogerwerf, R., de Bruijne, J. H. J., Brown, A. G. A., & Blaauw, A. 1999, AJ, 117, 354
Dohlen, K., Langlois, M., Saisse, M., et al. 2008, Proc. SPIE, 4014, 70143L
Donati, J.-F., Gregory, S. G., Montmerle, T., et al. 2011, MNRAS, 417, 1747
Fedele, D., Tazzari, M., Booth, R., et al. 2017, arXiv:1711.05185
Follette, K. B., Grady, C. A., Swearingen, J. R., et al. 2015, ApJ, 798, 132
Frasca, A., Biazzo, K., Alcalá, J. M., et al. 2017, A&A, 602, A33
Fukagawa, M., Tamura, M., Itoh, Y., et al. 2006, ApJL, 636, L153
Gahm, G. F., Petrov, P. P., & Stempels, H. C. 2005, in ESA Special Publication 560, 13th Cambridge Workshop on Cool Stars, Stellar Systems and the Sun, ed. F. Favata, G. A. J. Hussain, & B. Battrick (Les Ulis: ESA), 563
Gaia Collaboration, Brown, A. G. A., Vallenari, A., et al. 2018, arXiv:1804.09365
Garufi, A., Benisty, M., Stolker, T., et al. 2017a, Msngr, 169, 32
Garufi, A., Meeus, G., Benisty, M., et al. 2017b, A&A, 603, A21
Garufi, A., Quanz, S. P., Schmid, H. M., et al. 2014, A&A, 568, A40
Garufi, A., Quanz, S. P., Schmid, H. M., et al. 2016, A&A, 588, A8
Ginski, C., Stolker, T., Pinilla, P., et al. 2016, A&A, 595, A112
Günther, H. M., Matt, S. P., Schmitt, J. H. M. M., et al. 2010, A&A, 519, A97
Hashimoto, J., Dong, R., Kudo, T., et al. 2012, ApJL, 758, L19
Hashimoto, J., Tamura, M., Muto, T., et al. 2011, ApJL, 729, L17
Hauschildt, P. H., Allard, F., & Baron, E. 1999, ApJ, 512, 377
Herczeg, G. J., Walter, F. M., Linsky, J. L., et al. 2005, AJ, 129, 2777
Huang, J., Öberg, K. I., & Andrews, S. M. 2016, ApJL, 823, L18
Huang, J., Öberg, K. I., Qi, C., et al. 2017, ApJ, 835, 231
Hughes, J., Hartigan, P., & Clampitt, L. 1993, AJ, 105, 571
Ingleby, L., Calvet, N., Herczeg, G., et al. 2013, ApJ, 767, 112
Johns-Krull, C. M., Valenti, J. A., & Linsky, J. L. 2000, ApJ, 539, 815
Kastner, J. H., Hily-Blant, P., Sacco, G. G., Forveille, T., & Zuckerman, B. 2010, ApJL, 723, L248
Kastner, J. H., Sacco, G. G., Montez, R., et al. 2011, ApJL, 740, L17
Kenyon, S. J., & Hartmann, L. 1987, ApJ, 323, 714
Keppler, M., Benisty, M., Müller, A., et al. 2018, A&A, submitted
Kooistra, R., Kamp, I., Fukagawa, M., et al. 2017, A&A, 597, A132
Krautter, J., Wichmann, R., Schmitt, J. H. M. M., et al. 1997, A&AS, 123, 329
Lamzin, S. A., Bisnovatyi-Kogan, G. S., Errico, L., et al. 1996, A&A, 306, 877
Lommen, D., Wright, C. M., Maddison, S. T., et al. 2007, A&A, 462, 211
Lommen, D. J. P., van Dishoeck, E. F., Wright, C. M., et al. 2010, A&A, 515, A77
Long, Z. C., Fernandes, R. B., Sitko, M., et al. 2017, ApJ, 838, 62
Langlois, M., Dohlen, K., Vigan, A., et al. 2014, Proc. SPIE, 9147, 91471R
Makarov, V. V. 2007, ApJ, 658, 480
Mamajek, E. E., & Bell, C. P. M. 2014, MNRAS, 445, 2169
Manara, C. F., Testi, L., Natta, A., et al. 2014, A&A, 568, A18
Marino, S., Perez, S., & Casassus, S. 2015, ApJL, 798, L44
Mayama, S., Hashimoto, J., Muto, T., et al. 2012, ApJL, 760, L26
Mawet, D., Absil, O., Montagnier, G., et al. 2012, A&A, 544, A131
Meeus, G., Waters, L. B. F. M., Bouwman, J., et al. 2001, A&A, 365, 476
Merín, B., Brown, J. M., Oliveira, I., et al. 2010, ApJ, 718, 1200
Miotello, A., van Dishoeck, E. F., Williams, J. P., et al. 2017, A&A, 599, A113
Monnier, J. D., Harries, T. J., Aarnio, A., et al. 2017, ApJ, 838, 20
Mullally, F., Coughlin, J. L., Thompson, S. E., et al. 2015, ApJS, 217, 31
Murphy, S. J., Lawson, W. A., & Bessell, M. S. 2013, MNRAS, 435, 1325
Muto, T., Grady, C. A., Hashimoto, J., et al. 2012, ApJL, 748, L22
Nuernberger, D., Brandner, W., Yorke, H. W., & Zinnecker, H. 1998, A&A, 330, 549
Öberg, K. I., Furuya, K., Loomis, R., et al. 2015, ApJ, 810, 112
Öberg, K. I., Qi, C., Fogel, J. K. J., et al. 2011, ApJ, 734, 98
Oh, D., Hashimoto, J., Carson, J. C., et al. 2016a, ApJL, 831, L7
Oh, D., Hashimoto, J., Tamura, M., et al. 2016b, PASJ, 68, L3
Ohta, Y., Fukagawa, M., Sitko, M. L., et al. 2016, PASJ, 68, 53
Olofsson, J., Samland, M., Avenhaus, H., et al. 2016, A&A, 591, A108
Owen, J. E. 2016, PASA, 33, e005
Padgett, D. L., Cieza, L., Stapelfeldt, K. R., et al. 2006, ApJ, 645, 1283
Panić, O., Hogerheijde, M. R., Wilner, D., & Qi, C. 2009, A&A, 501, 269
Pérez, L. M., Carpenter, J. M., Chandler, C. J., et al. 2012, ApJL, 760, L17
Pinte, C., Menard, F., Duchene, G., et al. 2017, arXiv:1710.06450
Pinte, C., Padgett, D. L., Ménard, F., et al. 2008, A&A, 489, 633
Podio, L., Garcia, P. J. V., & Bacciotti, F. 2007, MmSAI, 78, 693
Pohl, A., Benisty, M., Pinilla, P., et al. 2017, ApJ, 850, 52
Quast, G. R., Torres, C. A. O., de La Reza, R., da Silva, L., & Mayor, M. 2000, in IAU Symp. 200, The Formation of Binary Stars, Birth and Evolution of Binary Stars, ed. Bo Reipurth & Hans Zinnecker (Cambridge: Cambridge Univ. Press), 28
Rapson, V. A., Kastner, J. H., Andrews, S. M., et al. 2015a, ApJL, 803, L10
Rapson, V. A., Sargent, B., Germano Sacco, G., et al. 2015b, ApJ, 810, 62
Rodriguez, D. R., Kastner, J. H., Wilner, D., & Qi, C. 2010, ApJ, 720, 1684
Romero, G. A., Schreiber, M. R., Cieza, L. A., et al. 2012, ApJ, 749, 79
Rosenfeld, K. A., Andrews, S. M., Wilner, D. J., Kastner, J. H., & McClure, M. K. 2013, ApJ, 775, 136
Rosenfeld, K. A., Andrews, S. M., Wilner, D. J., & Stempels, H. C. 2012, ApJ, 759, 119
Schneider, G., Grady, C. A., Hines, D. C., et al. 2014, AJ, 148, 59
Schütz, O., Meeus, G., & Sterzik, M. F. 2005, A&A, 431, 165
Siess, L., Dufour, E., & Forestini, M. 2000, A&A, 358, 593
Siwak, M., Ogloza, W., Rucinski, S. M., et al. 2016, MNRAS, 456, 3972
Stempels, H. C., & Gahm, G. F. 2004, A&A, 421, 1159
Stempels, H. C., Gahm, G. F., & Petrov, P. P. 2007, A&A, 461, 253
Stempels, H. C., & Piskunov, N. 2002, A&A, 391, 595
Stolker, T., Dominik, C., Avenhaus, H., et al. 2016, A&A, 595, A113
Stolker, T., Sitko, M., Lazareff, B., et al. 2017, ApJ, 849, 143
Takami, M., Bailey, J., & Chrysostomou, A. 2003, A&A, 397, 675
Takami, M., Karr, J. L., Hashimoto, J., et al. 2013, ApJ, 772, 145
Tazzari, M., Testi, L., Ercolano, B., et al. 2016, A&A, 588, A53
Thalmann, C., Mulders, G. D., Janson, M., et al. 2015, ApJL, 808, L41
Tinbergen, J. 2005, Astronomical Polarimetry (Cambridge: Cambridge Univ. Press)
Torres, C. A. O., Quast, G. R., Melo, C. H. F., & Sterzik, M. F. 2008, in Handbook of Star Forming Regions, Vol. II: The Southern Sky, ed. B. Reipurth (San Francisco, CA: ASP), 757
van Boekel, R., Henning, T., Menu, J., et al. 2017, ApJ, 837, 132
van der Marel, N., van Dishoeck, E. F., Bruderer, S., et al. 2016, A&A, 585, A58
van der Marel, N., van Dishoeck, E. F., Bruderer, S., Pérez, L., & Isella, A. 2015, A&A, 579, A106
van der Plas, G., Ménard, F., Canovas, H., et al. 2017, A&A, 607, A55
van Kempen, T. A., van Dishoeck, E. F., Brinch, C., & Hogerheijde, M. R. 2007, A&A, 461, 983
Wagner, K., Apai, D., Kasper, M., & Robberto, M. 2015, ApJL, 813, L2
Williams, J. P., & Cieza, L. A. 2011, ARA&A, 49, 67
Wolff, S. G., Perrin, M., Millar-Blanchaer, M. A., et al. 2016, ApJL, 818, L15